

H-93
E7067

NASA Technical Memorandum 105687

Supersonic Investigation of Two-Dimensional Hypersonic Exhaust Nozzles

Jeanne D. Carboni and Rickey J. Shyne
Lewis Research Center
Cleveland, Ohio

and

Laurence D. Leavitt, John G. Taylor, and Milton Lamb
Langley Research Center
Hampton, Virginia

October 1992

NASA

SUPERSONIC INVESTIGATION OF TWO-DIMENSIONAL HYPERSONIC EXHAUST NOZZLES

Jeanne D. Carboni and Rickey J. Shyne
National Aeronautics and Space Administration
Lewis Research Center
Cleveland, Ohio 44135-3191

and

Laurence D. Leavitt, John G. Taylor, and Milton Lamb
National Aeronautics and Space Administration
Langley Research Center
Hampton, Virginia 23665-5225

SUMMARY

E-7067

An experimental investigation was conducted in the NASA Lewis Research Center 10-Foot by 10-Foot Supersonic Wind Tunnel to determine the performance characteristics of two-dimensional hypersonic exhaust nozzles/afterbodies at low supersonic conditions. Generally, this type of application requires a single expansion ramp nozzle (SERN) that is highly integrated with the airframe of the hypersonic vehicle. At design conditions (hypersonic speeds), the nozzle generally exhibits acceptable performance. At off-design conditions (transonic to mid-supersonic speeds), nozzle performance of a fixed geometry configuration is poor. Various two-dimensional nozzle configurations were tested at off-design conditions from Mach 2.0 to 3.5. Performance data is presented at nozzle pressure ratios from 1 to 35. Jet exhaust was simulated with high-pressure air. To study performance of different geometries, nozzle configurations were varied by interchanging the following model parts: internal upstream contour, expansion ramp, sidewalls, and cowl.

Results indicated that the following configurations performed better than others over the range of test conditions: short sidewalls, long expansion ramps, long straight (undeflected) cowls, and large internal expansions. Best overall performance was achieved by the NASA baseline configuration, a geometry containing a long curved ramp, short sidewalls and internal expansion ratio of 1.2.

The experiment yielded slightly different results from a previous test at transonic conditions (ref. 1), but similar trends were observed. In general, the nozzles exhibited poor performance in the transonic to low supersonic speed regime.

INTRODUCTION

Current focus on high-speed aircraft has renewed interest in the design and operation of a propulsion system to meet the mission requirements of hypersonic flight and single-stage-to-orbit (SSTO). The airframe of a typical SSTO vehicle usually includes a highly-integrated advanced propulsion system. One particular type of hypersonic exhaust nozzle is a two-dimensional single expansion ramp in which the aft undersurface of the aircraft provides the expansion surface for the nozzle flow. Unfortunately, these nozzle geometries tend to produce a significant amount of vehicle drag at transonic and mid-supersonic speeds.

An investigation previously conducted in the NASA Langley Research Center 16-Foot Transonic Wind Tunnel determined the performance of hypersonic exhaust nozzles at subsonic and transonic speeds.

The study revealed significant drag losses for this type of nozzle (ref. 1). This report presents experimental performance data of the same nozzles at low supersonic speeds in the NASA Lewis 10-Foot by 10-Foot Supersonic Wind Tunnel. (Reference 2 presents some of the typical nozzle expansion surface pressure distributions that were obtained from the experiment.) The two tests involved parametric investigations of the nozzle geometry. The effects of the following variables were studied: sidewall length and shape; cowl length, internal expansion ratio, and boattail angle; and ramp length and curvature. The geometries were altered by changing model hardware.

APPARATUS AND PROCEDURE

Description of 10-Foot by 10-Foot Supersonic Wind Tunnel

Model testing was conducted in the NASA Lewis 10-Foot by 10-Foot Supersonic Wind Tunnel (ref. 3). The model was located in the forward part of the tunnel test section to allow schlieren flow visualization of the exhaust plume. Jet exhaust was simulated by high-pressure air supplied from the NASA Lewis central air system. The high-pressure air system contained valves, filters, and a heat exchanger for air temperature control. Both the facility and the model were remotely operated and monitored from a control room, which contained the model airflow valve control system, the data acquisition system, and the television and schlieren system video monitors for observation of the model and the jet plume.

Nozzle Jet Simulation Rig

Figure 1 is a brief schematic of the nozzle jet simulation rig. The location of the forebody, low-pressure plenum, instrumentation section, and nozzle section are indicated in the top view of the isolated afterbody/nozzle model (fig. 1(a)). The side view (fig. 1(b)) illustrates both the location of the metric break of the six-component force balance system and the sting/strut assembly used for tunnel installation. Figures 2(a) and (b) are photographs of the rig mounted in the wind tunnel test section. The front view (fig. 2(a)) shows one of the schlieren system optical windows behind the forebody of the model. The rear view (fig. 2(b)) shows one of the exhaust nozzle configurations, specifically the long curved $17^\circ/8^\circ$ expansion ramp with short sidewalls and short cowl. Below the model is the sting/strut assembly.

For jet exhaust simulation, a high-pressure air system, external to the tunnel, provided a continuous flow of air at a temperature of approximately 75°F . Nozzle pressure ratios up to 190 could be obtained by pressure variation of this air. Figure 3 is a schematic of the jet exhaust simulation test rig. The model was mounted from the tunnel floor by a sting/strut assembly, which enclosed the air and instrumentation lines. The air was supplied through a line in the strut to a high-pressure plenum chamber within the test rig. From there, the air was perpendicularly discharged into a low-pressure plenum through eight, equally spaced, sonic nozzles located radially around the high-pressure plenum. This procedure minimized the forces produced by transfer of axial momentum as air passed from the nonmetric to the metric section of the force balance. Sealing the airflow between the nonmetric and metric parts of the rig was a pair of flexible metal bellows that compensated for any axial force caused by pressurization of the balance. From the low-pressure plenum, the air passed through a circular-to-rectangular transition section, a rectangular flow straightener (choke plate), a rectangular instrumentation section, and into the nozzle. The nozzle inlet (nozzle-connect station) marked the point of the model after which the hardware became configuration-dependent. All of the various nozzle model components (upstream plug, nozzle ramp, sidewalls, and cowl) connected to the model at this axial station.

Because the strut mounted from the tunnel floor, all of the air and instrumentation lines were located below the model. To facilitate frequent assembly and disassembly of nozzle hardware and to minimize the strut impact on the nozzle ramp flow, the test nozzle configurations were mounted on the rig upside-down from the typical flight position on a vehicle. In the results section, all nozzle diagrams (with the exception of figs. 1 to 3) and performance results are presented as though the nozzle was positioned along the undersurface of a hypersonic aircraft.

Nozzle Model Configurations

The test configurations were two-dimensional single expansion ramp nozzles (SERN's). They had nonaxisymmetric geometries with throat areas of nominally 8 in.², lengths varying from 15 to 22 in., and various internal expansion profiles. Each nozzle model was comprised of the following pieces of hardware: an upstream plug, an expansion ramp, two sidewalls, and a cowl. The upstream plug, in conjunction with the cowl and sidewalls, provided a specific internal nozzle contour. The expansion ramp provided a specific internal-to-external nozzle contour. Every configuration had a consistent arrangement of the four basic components as illustrated in figure 4, which shows the NASA baseline configuration. Figure 5 details the geometry of each expansion ramp with its respective upstream contour. Figures 6 and 7 show the various sidewall and cowl geometries. Table I summarizes the test configurations presented in this report.

The NASA baseline configuration (fig. 4) had the following geometry: the long curved 17°/8° ramp (fig. 5(a)), short sidewalls, convergent-divergent upstream contour, and short cowl 3 which provided an internal expansion ratio, ϵ_i , of 1.2. The ramp shape was a skewed parabola with an initial angle of 17° and a trailing edge angle of 8° (chordal angle of 11°). Its length, l , the distance from nozzle-connect station to trailing edge, was 21.278 in. In comparison, the other three ramps had the following geometries: the long straight ramp (fig. 5(b)) had a constant slope of 11° and length of 21.278 in.; the short curved ramp (fig. 5(c)) had a cubic polynomial shape with initial angle 25°, trailing edge angle 6° (chordal angle of 16°), and length 15.021 in.; the short straight ramp (fig. 5(d)) had a constant slope of 16° and length of 15.021 in.

Four different sidewall geometries could be installed (fig. 6): short and long rectangular, partial triangular, and full triangular. The short and long rectangular sidewalls terminated at the respective short or long cowl trailing edge to complete the ducted portion of the nozzle. Both the partial and full sidewalls were triangular in shape. The partial sidewalls extended to approximately 70 percent of the length of the external portion of the nozzle (approximately 15 in. from the nozzle-connect station). The full sidewalls extended to the end of the external nozzle (21.278 in.).

Seven different cowl geometries were installed so that three major comparisons could be made: the effect of varying ϵ_i (the ratio of the air-flow exit area to the throat area), the effect of extending the nominal cowl geometry, and the effect of varying boattail angle. Figure 7(a) shows the five cowls used in the first two comparisons. Short cowls 1 through 4 (ϵ_i of 1.0, 1.1, 1.2, and 1.3, respectively) were installed with the short rectangular sidewalls. Each short cowl had a different contour downstream of the throat producing the four different internal expansions. The extended cowl was a slightly longer version of the short cowl geometry. It had an internal expansion ratio of 1.25 and was installed on the model with the long rectangular sidewalls. Boattail angle effects were studied with the two cowls shown in figure 7. The long straight cowl had an internal expansion ratio of 1.5. The long upturned cowl had no internal expansion ($\epsilon_i = 1.0$) and was angled upward at approximately 30°. Both of these long cowls were also installed with long sidewalls. The configuration containing the upturned cowl was essentially a

convergent nozzle up to the cowl exit plane, whereas the straight cowl provided a convergent-divergent geometry.

Instrumentation

A six-component strain-gage balance was used to measure the forces and moments of the model downstream of station 26.5 (fig. 3). The force balance was capable of measuring axial force up to 600 lb in the positive and negative directions, normal force up to 800 lb in the positive and negative directions, and pitching moment up to 4000 in.-lb in the positive and negative directions. The nozzle geometries were expected to produce primarily axial force (thrust/drag), normal force (lift), and pitching moment. As expected, only small fluctuations were noticed in roll moment, yaw moment, and side force. According to specifications, the accuracy of the force balance was ± 0.5 percent of the full scale loads for each component listed above.

Temperature and pressure measurements were made in the high-pressure plenum in order to determine the weight flow of the high-pressure air supplied to the nozzle (the weight flow calculation was calibrated with standard axisymmetric nozzles). Additional rig instrumentation was installed in a fixed instrumentation section (fig. 3). Three five-probe rakes distributed across the plenum measured jet total pressure. A thermocouple installed on the center rake measured jet total temperature. Of the interchangeable model hardware, instrumentation was located only on the ramp and upstream plug. Both were instrumented to measure nozzle surface static pressure. The internal surface of each upstream plug contained 13 static pressure orifices spaced at half-inch intervals along the centerline. For Lewis test configurations, only three of these pressure taps were used (taps 1, 6, and 12, in order starting from the furthest upstream position). Along the inside surface of the expansion ramp, there were four rows of 22 static pressure orifices spaced 1 in. apart (in the axial direction). For the Lewis test, only 28 of these ramp pressures were used, 14 along the centerline row and 14 along the outermost row. Figure 8 gives the positions of the static pressure taps along the upstream plug and ramp surface for each configuration. Axial positions are described in the form x/l , where l is the nozzle ramp length of the specific configuration (previously defined, from nozzle-connect station to trailing edge) and x is the axial distance downstream from the nozzle-connect station (fig. 8). The parameter $y/(w/2)$ describes the lateral (y -direction) location of the pressure taps outward from the centerline of the ramp. Each ramp had a width of approximately 8 in. The centerline taps were at a y -position of zero and the outboard taps were approximately 3 in. off-center (fig. 8).

Data Reduction

The data for this test was recorded on an Escort III data acquisition system which updated in real time at a rate of one scan/sec. For each steady-state point, the average value of five scans (5 sec) of data was calculated and stored for analysis and reprocessing after the test. Data was recorded for increasing values of nozzle pressure ratio (NPR) at tunnel freestream Mach numbers of 0.0, 2.0, 2.5, 3.0, and 3.5. NPR is the ratio of average jet total pressure, $p_{t,j}$, measured in the model instrumentation section, to tunnel freestream static pressure, p_0 . Tunnel freestream total pressure, $p_{t,0}$, was held constant at 1950 psf for all Mach numbers. Nozzle jet total temperature, $T_{t,j}$, was maintained between 65 and 75 °F during NPR sweeps. Before recording each data point, the model was positioned at a zero angle of attack.

The following basic performance parameters were determined from the investigation: nozzle discharge coefficient, C_d ; internal thrust ratio, F_G/F_I ; thrust vector angle, δ ; thrust-minus-drag ratio, $(F-D)/F_I$; thrust-removed drag coefficient, C_{D_i} ; lift ratio, L/F_I ; and expansion ramp surface pressure

ratio, $p/p_{t,j}$, or pressure coefficient, C_p . Nozzle discharge coefficient, C_d , quantitatively shows the ability of the nozzle to deliver weight flow (ref. 5). It is the ratio of measured weight-flow rate, W_p , to ideal weight-flow rate, W_I , where ideal weight-flow was based on jet total pressure, $p_{t,j}$, and temperature, $T_{t,j}$, and the measured nozzle throat area, A_t . The internal gross thrust ratio, F_G/F_I , is the ratio of actual nozzle thrust to ideal nozzle thrust at wind-off (no tunnel flow) conditions. Ideal nozzle thrust was calculated assuming isentropic expansion of a perfect gas at the measured nozzle weight-flow and jet total pressure and temperature. The actual nozzle thrust, F_G , was computed from the balance axial and normal force measurements.

A detailed description of the force balance data reduction equations is in reference 4. A very brief description will be given here. The force measurement was initially corrected for model weight tares and balance interactions, then corrected for pressure and momentum tare forces.

Although the internal bellows assembly of the balance was designed to remove pressure and momentum interactions in the balance, small bellows tares on the six balance forces and moments still remained. When the bellows assembly is pressurized, a pressure tare can result from a small difference in the forward and aft bellows spring constants. At high internal velocities, a momentum tare can result from a small pressure difference between the ends of the bellows. Pressure tare corrections were determined by pressurizing the model. Momentum tare corrections were determined by installing an axisymmetric calibration nozzle that had a throat area, A_t , of 8.513 in.² to approximate the throat area of the nozzle test configurations. The calibration nozzle, which had a thrust performance that was previously documented, was tested on the rig at Lewis over a range of normal force and pitching moment loading conditions. These loading conditions defined flow momentum corrections based on the initial weight (preload) of each model configuration. Nozzle axial force, normal force, and pitching moment were obtained after the raw balance data was corrected for all of the interactions and tare forces.

Performance parameters were computed from the corrected balance data. Thrust and thrust vector angle were determined at static conditions. Net thrust ratio $(F-D)/F_I$, was obtained from the axial force at wind-on conditions. For each configuration tested, knowledge of the thrust level for a given NPR at wind-off conditions yielded the thrust-removed drag coefficient, C_D ($D/q_0 A_{ref}$, where D is the thrust-removed drag, q_0 is the freestream dynamic pressure, and A_{ref} is the largest upstream area in the model.) The static (tunnel-off) conditions yielded information for calculating thrust-removed drag: at a given NPR and M_0 , D is equal to measured net thrust (from the balance data) minus the static thrust ($M_0 = 0$) generated at the same NPR. Lift (and the resulting lift ratio) was obtained from balance normal force. All of the data reduction equations are in reference 4.

The last performance parameters presented in the results are static pressure ratio, $p/p_{t,j}$, and pressure coefficient, C_p , both obtained from the static pressure taps along the nozzle ramp surface. C_p is the ratio of the difference between ramp surface pressure (p) and freestream static pressure (p_0) to the freestream dynamic pressure (q_0). To compare each expansion ramp, C_p was plotted as a function of x/l , the axial distance from the nozzle-connect station normalized by the ramp length, l . For static conditions, q_0 was zero, so the pressure ratio $p/p_{t,j}$ was plotted instead of C_p .

RESULTS AND DISCUSSION

Nozzle thrust performance was measured for both wind-off (no tunnel flow) and wind-on conditions at tunnel freestream Mach numbers of 2.0, 2.5, 3.0, and 3.5. Static internal performance data was acquired at a tunnel ambient pressure of 400 psf. Installed performance data was obtained at a tunnel freestream total pressure of 1950 psf. Table II contains the Mach number-NPR schedule representing a

typical hypersonic vehicle trajectory for speeds up to Mach 3.5. Installed data and ramp pressure distributions were plotted for these trajectory points.

As previously stated, force data, descriptions, and sketches have been corrected so that the nozzle is oriented in a "flight" position (upside-down from the way in which it was mounted in the tunnel) along the undersurface of an aircraft with the cowl located below the nozzle ramp. Previous diagrams (except figs. 1 to 3) were oriented in this manner which will allow the following sign conventions to be used for forces on the model (fig. 9): positive normal force (lift) pointed upward, positive axial force (thrust) pointed upstream, and thrust vector angle was positive in the upward direction.

Static Performance Comparison

Discharge coefficient and thrust ratio are two variables frequently used to measure static (wind-off) internal performance of nozzles. In this particular investigation, these two parameters were used not only to compare small performance differences among the many nozzle configurations, but also to compare performance differences of the same nozzle between the two facilities in which they were tested. Internal nozzle performance was measured at wind-off conditions in both the Langley 16-Foot Transonic Wind Tunnel and the Lewis 10-Foot by 10-Foot Supersonic Wind Tunnel. Ideally, the static performance of a model in one tunnel would agree with its static performance in another tunnel as long as pressure and temperature conditions were the same. However, small differences were found in both the discharge coefficient and the static thrust ratio of the model between the two test facilities.

The measured weight flow (W_P), in the numerator of the discharge coefficient (C_d), was calculated by a different method in each facility. At Langley, choked venturis were used to measure the weight flow of the air passing through the model. At Lewis, using choked venturis would have decreased the amount of internal airflow available, so they were not installed in the air line. Instead, model plenum chamber pressure and temperature measurements were used to calculate weight flow. The previous section of this report briefly described the weight flow calculation method used at Lewis, and reference 4 presents it in detailed equations. The two different flow measuring techniques appeared to produce a discrepancy at static conditions between the two facilities. Figure 10 shows that, for a sample of four configurations tested, Langley consistently computed a discharge coefficient approximately 2 percent higher than Lewis.

This small discrepancy in static discharge coefficient translated into an associated small discrepancy in the static thrust ratio (F_G/F_I). Figure 11 illustrates the difference in F_G/F_I for the same four configurations shown in figure 10. At static conditions, the Langley test generated thrust at a level approximately 2 percent lower than the Lewis test. Based on the equations used to calculate the two variables, this discrepancy in static thrust ratio was a direct consequence of the deviation in C_d . The ideal thrust, F_I , in the denominator of the static thrust ratio is directly proportional to the measured weight flow, W_P :

$$F_I = W_P \sqrt{\frac{R_j T_{t,j}}{g_c} \left(\frac{2\gamma_j}{\gamma_j - 1} \right) \left[1 - \left(\frac{1}{P_{t,j}} \right)^{\frac{\gamma_j - 1}{\gamma_j}} \right]}$$

where γ_j is the specific heat ratio of the jet ($\gamma = 1.3997$ for air), R_j is the specific gas constant of the jet ($R_j = 53.364 \text{ ft}^2/\text{R}$ for air), and g_c is the gravitational constant. This equation depicts an inverse relationship between C_d and F_G/F_I . Therefore, a discrepancy in C_d would have caused an opposite but consistent discrepancy in F_G/F_I between the two test facilities.

A 2-percent variation in discharge coefficient is not unusual when two separate flow measurement techniques are used. Possible dissimilarities in test facilities were complicated by the dismantling and reassembly of the jet-exit model and force balance between the two tests. These factors were used to explain the discrepancy in the two sets of data.

Performance of Baseline Configuration

The NASA baseline configuration was composed of the following hardware: the long curved $17^\circ/8^\circ$ ramp, short sidewalls, convergent-divergent upstream plug, and short cowl 3 ($\epsilon_1 = 1.2$). This configuration was used for initial testing in both the Langley Transonic Wind Tunnel and the Lewis 10-Foot by 10-Foot Supersonic Wind Tunnel. Its performance was investigated over the entire range of speeds from subsonic to low supersonic (Mach 0.0 to 3.5). Figure 12 shows net thrust ratio (i.e., thrust-minus-drag ratio) as a function of nozzle pressure ratio for all the Mach numbers tested, including static conditions. Data obtained from Langley (ref. 1), represents freestream conditions of Mach 0, 0.6, 0.8, 0.9, 0.95, and 1.2. Data from Lewis, represents freestream Mach numbers of 2.0, 2.5, 3.0, and 3.5. The dashed line indicates the characteristic hypersonic vehicle trajectory of points specified in table II.

At each freestream Mach number, the net thrust showed an expected increase with nozzle pressure ratio, and the peak nozzle performance shifted toward higher nozzle pressure ratios as the Mach number increased. These trends were consistently demonstrated by both the Langley and Lewis results. Figure 12 also revealed that maximum net thrust ratio decreased as the Mach number increased up to approximately Mach 2.0, after which it settled near a value of 0.8. The causes of this low nozzle performance will be discussed later in the report. Generally, nozzle pressure ratios available in current standard hypersonic engine cycles (indicated by the dashed line) are less than the peak values shown. Combined with low overall nozzle performance, this may necessitate thrust augmentation at low Mach numbers for this specific type of hypersonic nozzle.

One objective of the Lewis test was to extend the speed range of the database that had previously been generated at Langley. Figure 13 shows performance of the baseline configuration for the entire range of Mach numbers tested. In figures 13(a) and (b), net thrust ratio and thrust-removed drag coefficient are plotted for the trajectory points defined by both table II and the dashed line in figure 12. Figure 13(a) shows that the transonic drag rise caused a rapid decrease in net thrust, followed by only a gradual increase from Mach 2 to 3.5 as nozzle pressure ratio increased. This evidence demonstrates again that the performance of this nozzle is generally poor at transonic and low supersonic conditions. In figure 13(b), the drag coefficient showed an expected rapid increase in drag around Mach 1.0, followed by a steady decrease with increasing Mach number. At jet-off conditions (no internal flow), the drag of the model appeared to level off after Mach 1.0. At jet-on conditions (scheduled NPR), the drag coefficient became negative around Mach 2.75, indicating an additional "thrust" at higher Mach numbers. This favorable jet-effect can be experienced by exhaust nozzles when their geometry enables the jet plume to pressurize the boattail at high NPR's. However, because pressure instrumentation was not available (had not been installed) along the external surface of the cowl, existence of this boattail pressurization effect could not be confirmed, and only the baseline configuration showed evidence of it.

Ramp pressure distributions are shown in figure 14 for both static and installed conditions. For static conditions (fig. 14(a-1)), $p/p_{t,j}$ was plotted as a function of axial distance along the ramp for both the centerline and out-board pressure taps. The plot illustrates a large overexpansion immediately downstream of the cowl trailing edge, after which the flow separated from the ramp surface, and the ramp

pressures settled out near tunnel ambient pressure. The flow separation was evident in schlieren photographs (fig. 14(a-2)) and video tapes that were taken during the test. This result is typical of a SERN nozzle.

Ramp pressure distributions at the four test Mach numbers (NPR's from table II) are plotted in figures 14(b) to (e). Schlieren photographs (figs. 14(b-2) and (d-2)) are included to illustrate two of the highly complex flowfields that were seen in the nozzle: one at a low Mach number, low NPR condition and the other at a high Mach number, high NPR condition. The y-axis parameter in the four graphs is the ramp surface pressure coefficient (C_p), which illustrates pressure drag on the nozzle for installed conditions better than the pressure ratio $p/p_{t,j}$. C_p values below zero result in drag on the ramp, and values above zero produce a thrust force. At Mach 2, figure 14(b-1) shows that the overexpansion still existed along the centerline directly downstream of the cowl exit plane, after which the curved ramp surface recompressed the flow to a pressure slightly above tunnel static (p_0). The flow appeared to separate downstream of the recompression and then settle out to p_0 . The outboard pressures generally remained below p_0 , except for the two orifices furthest upstream, demonstrating a slight three-dimensional effect. The schlieren photograph in figure 14(b-2) shows an internal shock and an external shock that both originated at the cowl trailing edge. The internal shock reflected off the ramp surface and caused a boundary layer separation. As Mach number and NPR increased (figs. 14(c) to (e)), the pressure distribution stretched out—both the initial overexpansion and the separation were pushed downstream, and the centerline and out-board pressures came into closer agreement as the higher pressure flow filled up more of the nozzle volume. The schlieren photograph of figure 14(d-2) illustrates the change in the nozzle flowfield from low NPR to high NPR conditions: the shock structure and shear layer were pushed outward and there may have been a slight flow separation toward the aft part of the ramp surface. The result was a reduction in the overall nozzle drag at higher Mach numbers and NPR's.

Sidewall Geometry Effects

The three sidewall geometries (short, partial, and full) were described in figure 6. They were installed with the long curved $17^\circ/8^\circ$ ramp and short cowl 3 ($\epsilon_1 = 1.2$). The short rectangular sidewalls extended to the end of the ducted portion of the nozzle (cowl trailing edge). The partial triangular sidewalls extended to approximately 70 percent of the length, and the full triangular sidewalls extended the entire length of the external nozzle.

Internal performance.—Static performance data was obtained for each sidewall configuration at NPR's from 1 to 12. Figure 15 illustrates the internal performance parameters, static thrust ratio and thrust vector angle. Although the performance of the three configurations was similar, figure 15(a) shows that the short and full sidewalls achieved slightly higher thrust levels at low NPR's, but the partial and full sidewalls were more effective at high NPR's. Figure 15(b) shows that the full sidewalls achieved the largest negative thrust vector angle. Fuller sidewalls produced a larger force in the normal direction by forcing the nozzle flow to expand mainly along the ramp surface and in a direction normal to it instead of spilling over the sides as with shorter sidewalls. As a result, the thrust was vectored at a larger angle. At high NPR's, the angle approached a value of zero, indicating that the plume was expanding outward instead of mainly along the ramp surface.

Installed performance.—Installed performance data (fig. 16) was plotted for the last four points in table II. Figure 16(a) shows the net thrust ratio of the three sidewall configurations. All three sidewall configurations demonstrated similar behavior and thrust level, resembling the static results. The short sidewalls achieved the best performance, but only by a very small margin. Figure 16(b) shows that the thrust-removed drag of the short sidewall configuration (the NASA baseline configuration) had a negative

value at Mach numbers above 2.75. The drag of the other two configurations was almost constant (only slightly decreasing) across the Mach number range. As discussed in the previous section, the negative C_D could have been the result of a boattail pressurization. In this comparison, increasing sidewall length seemed to reduce the favorable impact of NPR on boattail drag.

Ramp surface pressures.—Figure 17 compares centerline and off-centerline ramp pressure distributions of the three sidewall configurations for static and installed conditions (see table II). At all Mach numbers and NPR's, figures 17(a) to (e) indicate that the various sidewalls did not cause a considerable change in the nozzle centerline pressures. A typical SERN distribution existed, but there was almost no variation among the different sidewall configurations. The only difference among the three geometries was the length and shape of the sidewalls. Therefore, the pressure taps along the outboard edge of the ramp (i.e., very close to the sidewalls) were expected to show a greater difference than the centerline pressures in comparing the three configurations. However, the off-centerline ramp pressures showed that there was almost no influence of external flow, thus confirming the similarity of the thrust performance results. These results show that sidewall length and shape appeared to have a more significant effect on boattail pressure than on ramp surface pressure.

Cowl Geometry Effects

Various cowl geometries are described in figures 7(a) and (b). The cowl geometry changes were made to investigate the effects of varying internal expansion ratio, length, and boattail angle. The effects of changing the internal expansion were studied using four short cowls with internal expansion ratios (ϵ_i) of 1.0, 1.1, 1.2, and 1.3. The length comparison was made with short cowl 3 ($\epsilon_i = 1.2$) and the extended cowl ($\epsilon_i = 1.25$). The boattail angle comparison was made with the long straight cowl ($\epsilon_i = 1.5$) and the long upturned cowl ($\epsilon_i = 1.0$).

Internal Expansion Ratio

Each short cowl geometry contained a different internal expansion ratio upstream of the cowl trailing edge. The four cowl geometries were installed on the model with the long curved $17^\circ/8^\circ$ ramp and short sidewalls.

Internal Performance.—At static conditions, only slight differences existed among the four configurations. As expected, thrust curves peak at some intermediate NPR that varied with internal expansion ratio (fig. 18(a)). Close examination of figure 18(a) reveals that static thrust ratio increased at each NPR with increasing internal expansion ratio. Of the four short cowls, cowl 4 (ϵ_i of 1.3) achieved the best thrust performance, but only by a small margin. Figure 18(b) illustrates the static thrust vector angle of the four short cowl configurations. Again, they were in close agreement. For each cowl, there was a decreasing negative δ with increasing NPR. The cowl 4 configuration (ϵ_i of 1.3) exhibited the smallest (closest to zero) thrust vector angle at low NPR's, but the cowl 1 configuration (ϵ_i of 1.0) had the smallest angle for high NPR's. At low NPR's, a larger ϵ_i caused a larger flow expansion internally, therefore creating a more axially-directed thrust vector. At high NPR's, the thrust vector was governed primarily by the ramp flow because most of the expansion occurred externally. Therefore, at these high NPR conditions the highest upstream ramp pressures were achieved by cowl 1 which had the lowest ϵ_i . Because the upstream part of the ramp had a large effect on axial force, this configuration had the lowest thrust vector angle.

Installed performance.—Installed data was plotted for the last four points in the table II trajectory. At wind-on conditions, like wind-off, performance curves for the four configurations showed similar trends (fig. 19). However, in figure 19(a), the net thrust ratio of the geometry with no internal expansion (cowl 1, ϵ_i of 1.0) was noticeably lower than the other three. Figure 19(b) reveals that cowls 1, 2, and 4 demonstrated almost equal drag coefficients. But as before, negative drag values at high Mach numbers were achieved only by the baseline configuration (cowl 3, ϵ_i of 1.2).

Ramp surface pressures.—Figure 20 shows that varying the internal expansion ratio caused a noticeable difference in ramp pressures near the end of the internal nozzle at the cowl trailing edge ($x = 0$). Centerline pressures from $x/l = 0.2$ to $x/l = 1.0$ (the end of the ramp) were almost identical for all four configurations over the range of Mach numbers tested. However, upstream of that point, there is an obvious difference in the flow expansion.

The cowl 1 configuration (ϵ_i of 1.0) maintained internal surface pressures higher than the other three. At wind-off conditions, short cowl 1 showed evidence of a large overexpansion at the cowl exit plane (fig. 20(a)), whereas the other three configurations demonstrated large internal expansions (upstream of the cowl exit plane), apparent from their large pressure drop along the upstream plug surface. At all installed conditions, the cowl 1 configuration (no internal expansion) had upstream plug pressures higher than the other three. Internal surface pressures remained higher for decreasing internal expansions (figs. 20(a) to (e)). However, as the performance variables in figures 18(a) and 19(a) reveal, nozzle thrust was not significantly effected by these internal ramp pressures, mainly because the forward-facing area upon which they acted was very small. Therefore, the axial thrust did not deviate much among the four configurations because they all showed nearly the same ramp pressures just downstream of the exit plane, the region where the ramp projected area was large (resulting from the 17° initial angle). Geometrically, the ramp pressures would have had the largest influence on axial thrust in this region of the ramp surface.

All of the ϵ_i configurations had roughly the same sidewall and cowl boattail angles, and the ramp pressure distributions were extremely similar. This would indicate that the drag coefficient result for the cowl 3 configuration is not only the result of boattail pressurization effects.

Cowl Length

To investigate cowl length effects, an extended cowl was installed with long sidewalls (fig. 7(a)) and the long curved ramp. This configuration had an internal expansion ratio of 1.25. It was compared to the baseline configuration (containing short cowl 3), which had an internal expansion ratio of 1.2. The longer cowl had been designed to keep the flow from overexpanding too quickly after the nozzle throat (slightly upstream of the short-cowl exit plane).

Internal performance.—Static performance of the two cowls is compared in figure 21. Figure 21(a) shows that at wind-off conditions and low NPR's, the two configurations performed similarly, but at high NPR's the extended cowl performed better. The static thrust for both configurations peaked at roughly the same NPR (4.0). However, after the peak, the thrust ratio for the extended cowl remained at a higher level while the thrust ratio for the short cowl diminished at an increasing rate. Unlike the short cowls, the long cowl directed the expanding flow along the initial part of the ramp while it was still contained within the ducted nozzle, therefore raising the pressure along this surface. The result was a higher thrust at higher internal pressures. Figure 21(b) shows that the short cowl had a thrust vector closer to zero for high NPR's. One explanation is that for higher pressures, the long cowl forced the nozzle flow along the ramp at an initial 17° upward turn, therefore producing a larger negative normal force

on the model and "vectoring" the thrust at a larger negative angle. For lower NPR's, the two cowls had similar thrust vector angles.

Installed performance.—Wind-on performance data was again plotted for the last four points in the table II Mach number-NPR schedule. As the internal performance comparison showed, the longer cowl kept the nozzle flow from overexpanding at the start of the nozzle ramp. The results for installed conditions are shown in figure 22(a): the extended cowl had a better net thrust performance at all points in the trajectory. Figure 22(b) compares the drag of the two configurations. As before, the assumed boat-tail pressurization effect allowed a negative drag on the short cowl configuration (the baseline configuration). The extended cowl had an almost constant drag coefficient across the trajectory.

Ramp surface pressures.—Ramp centerline pressure distributions are shown in figure 23 for static and installed conditions. It is clear that the extended cowl delayed and, at installed conditions, reduced the overexpansion. Figure 23(a) illustrates that the flow expansion, recompression, and separation were all pushed downstream by the longer cowl at static conditions. Even though the two cowl geometries contained similar internal expansion ratios, the extended cowl maintained higher internal pressures because its internal expansion did not begin until the nozzle connect station (short-cowl exit plane). In the previous section, short cowl 1 (no internal expansion), which had the same internal geometry as the extended cowl up to the nozzle connect station, showed a very similar result (fig. 20(a)). At installed conditions (figs. 23(b) to (e)), the longer cowl provided an obvious rise in pressures along the upstream portion of the ramp. The flow was initially recompressed along the ramp, thus producing higher pressures near the 17° initial ramp angle. The higher pressures in this region resulted in a larger positive axial force which added to the thrust as explained earlier. The extended cowl also prevented a drag condition ($C_p < 0$) along the ramp centerline by maintaining the pressure above tunnel static, p_0 ($p = p_0$ corresponds to $C_p = 0$ on the ramp). The short cowl showed more evidence of ramp pressure drag at installed conditions.

Boattail Angle

The effect of a large external cowl boattail angle was studied by installing two long cowls, one with a straight contour and the other with a contour that was turned upward approximately 30° at the nozzle connect station. They were installed with the baseline ramp and long sidewalls, which terminated at the cowl trailing edge. The straight cowl had an internal expansion ratio of 1.5. The upturned cowl had no internal expansion (ϵ_1 of 1.0), therefore it was essentially a convergent nozzle.

Internal performance.—Figure 24(a) shows disagreement in the static performance of the two configurations. At low NPR's, the upturned cowl achieved higher thrust values than the straight cowl. At high NPR's (over six), the static thrust ratio of the upturned geometry steadily decreased to values below those of the straight geometry which increased to a peak then leveled off. Figure 24(b) yielded the following comparison: at low NPR's (below six), the static thrust vector angle of the two configurations behaved similarly, but at high NPR's, the upturned geometry produced a smaller negative angle (i.e., an angle closer to zero).

The above performance differences were understood after comparisons were made of all the static ramp pressure distributions for the two configurations (fig. 26(a) shows the distribution at an NPR of 2.0). At low NPR's, the upturned cowl produced higher thrust values because it pressurized the forward portion of the ramp by forcing the flow upward along the ramp surface before it exited. The straight geometry prevented this pressurization at low NPR's because the flow had already expanded around the 17° initial turn before the cowl exit plane. At high NPR's in the upturned geometry configuration, the

high-pressure internal flow was deflected upward, then forced to overexpand around the sharp cowl trailing edge, causing it to separate from the ramp surface immediately after it exited. The result of this separation was a large reduction in normal force along the aft part of the ramp, which caused a reduction in the overall gross thrust—the sum of axial force and normal force. This small normal force led to a small (almost zero) negative thrust vector angle because axial force was the remaining major component of the thrust vector. The straight cowl at high NPR's generated a higher static thrust because it allowed the plume to expand, contained at first, along the ramp surface and into a larger nozzle volume. The flow remained attached and generated lower-than-ambient pressures on the ramp surface, which resulted in a larger negative normal force. Therefore, the gross thrust vector increased in magnitude and had a larger negative angle.

Installed performance.—Installed performance data was plotted for the last four Mach numbers and NPR's shown in table II. The straight geometry exhibited better performance throughout the trajectory (fig. 25(a)). The net thrust curve of the straight geometry was approximately 5 to 7 percent higher than that of the upturned geometry. However, the two geometries exhibited a consistent trend of an increasing net thrust with increasing Mach number for the scheduled NPR. The upturned cowl's lower performance was caused by its higher boattail drag and an extremely complicated interaction of internal and external flow at its trailing edge.

Ramp surface pressures.—Ramp pressure distributions for points in table II are shown in figure 26. For a wind-off NPR of 2, figure 26(a) shows a significant difference in ramp pressures near the initial 17° ramp angle (just before the cowl exit plane). For the upturned cowl configuration, the internal flow remained at a higher pressure and did not overexpand at the cowl exit plane ($x/l \approx 0.1$). For the straight cowl, the flow expanded to below ambient pressure shortly after the throat (before the cowl exit) then slightly recompressed along the initial ramp surface. For wind-on conditions (figs. 26(b) to (e)) centerline pressures between the two configurations compared similarly at each Mach number. The upturned cowl still maintained a higher-pressure internal flow along the initial part of the ramp. However, downstream of the cowl exit plane near $x/l = 0.2$, the two configurations had the same distributions.

Both the thrust-removed drag plot and the surface pressure distributions did not show a large difference between the two configurations. Therefore, the following effect was probable: freestream tunnel flow along the external surface of the upturned cowl had already expanded around the cowl's turning angle and was either at a very low pressure or separated at the cowl trailing edge. This caused a large drag and lowered nozzle performance. When operating at off-design conditions (low Mach number and NPR), hypersonic SERN nozzle configurations usually experience a pressure drag at the forward part of the ramp from the overexpansion of internal flow. In effect, the upturned cowl configuration probably transferred this drag condition from the ramp to the external cowl surface. This assumption could not be verified because pressure taps had not been installed on the external cowl surface.

Ramp Geometry Effects

The various ramp geometries were described in figures 5(a) to (d). Ramp curvature effects were studied for both the two short ramps and the two long ramps. Ramp length effects were also investigated by comparing the short and long curved geometries.

Ramp Curvature – Short Ramps

The short curved $25^\circ/6^\circ$ ramp (16° chordal angle) was compared to the short straight 16° ramp. Both configurations had an internal expansion ratio of 1.0 (i.e., no internal expansion) and short sidewalls.

Internal performance.—At all static NPR's, the straight geometry generated a 2 to 3 percent higher thrust than the curved geometry (fig. 27(a)). The two configurations had similarly shaped but offset thrust curves which both peaked at about an NPR of 2.0 then slowly decreased as internal pressure increased. The thrust vector angle at static conditions is shown in figure 27(b). For the NPR's tested, the straight ramp swept through a larger range of angles than the curved ramp. The static thrust vector of the curved ramp remained near a value of -6° , its trailing edge angle. Of all four ramp geometries tested, the short straight ramp was the only one that had a positive thrust vector angle.

The difference in static performance of the two ramp geometries was better understood after a comparison was made of ramp surface pressure distributions (fig. 29(a)). The curved ramp's lower thrust resulted from its larger expansion immediately downstream of the cowl exit plane. In this region, the surface of the curved ramp had a larger projected area in the axial force direction that was acted upon by lower pressures than the straight ramp. Because of the large initial angle (25°) of the curved ramp, pressures on the surface remained low for a greater downstream distance than for the straight ramp. The curved surface also recompressed the flow to a pressure slightly above ambient for the remaining length. A significant decrease in overall thrust resulted. The straight ramp did not have as large an expansion at the cowl exit plane, and surface pressures almost immediately returned to ambient for the remaining length, probably resulting from a separation. At static conditions, it appeared that the reduced expansion rate of the straight ramp was more effective in producing overall thrust than the large expansion and recompression of the curved ramp.

At low NPR's, the smaller negative thrust vector angle of the curved ramp (fig. 27(b)) was the consequence of a slightly smaller ramp negative normal force. This smaller normal force resulted from the recompression along the aft part of the ramp surface. At high NPR's, the curved ramp's initial over-expansion decreased in magnitude and the ramp pressures showed a series of expansions and recompressions along the surface. Higher pressure flow was forced along the ramp and filled up more of the nozzle volume, causing the thrust vector angle to approach a value of -6° , the ramp's trailing edge angle. In contrast, the negative thrust vector angle of the straight ramp decreased steadily with NPR from about -13° to values near 0° . The primary cause of this decreasing angle was a change in the initial expansion. The higher pressure flow expanded into a larger volume, bounded on one side by the ramp at a 16° angle. The more symmetric flowfield caused a decrease in the negative normal component of the thrust vector.

Installed performance.—Because of time limitations and facility delays, the short straight ramp was not tested at Mach 3.0 and 3.5. Data for this ramp has been plotted only for Mach 2.0 and 2.5. The same trajectory as before (last four points in table II) was assumed. Contrary to the static results, figure 28(a) shows that the short curved ramp had better thrust performance at installed conditions. Figure 28(b) confirms that the installed drag of the straight ramp was slightly higher than the drag of the curved ramp.

Another variable used in comparing ramp curvature effects is lift (normal force). Figure 28(c) presents the ratio of lift to ideal thrust of the two configurations at installed conditions. Even though there is limited data, a trend shows that the straight ramp might have begun to generate a larger positive normal force than the curved ramp as Mach number and pressure ratio increased. Both configurations showed normal force increasing almost linearly with Mach number for the scheduled nozzle pressure

ratios. One reason for this was an increase in ramp surface pressure with Mach number and NPR. The centerline ramp pressures (figs. 29(b) to (e)) achieved values above ambient only at Mach 3.5, which just means that the forces on the ramp were in the positive normal and axial directions at that point. Before Mach 3.5, the pressures remained below ambient, causing negative normal and axial forces on that surface. (Surface pressures had a greater effect on normal force than on axial force because the projected area in the axial direction was almost negligible on the aft part of the ramp.) The pressure rise on the ramp was caused by high pressure flow not fully expanding to freestream conditions. At Mach 3.5, the lift ratio (fig. 28(c)) showed that the thrust vector had a positive normal component.

Ramp surface pressures.—Ramp centerline pressures were plotted for the straight and curved configurations in figures 29(a) to (e). Figures 29(d) and (e) contain pressures only for the curved configuration because the straight configuration was not tested at these conditions. The effect of the ramp centerline pressures on model forces was described in the previous section. Briefly, at static conditions (fig. 29(a)), the curved configuration contained an extended region of lower-than-ambient pressure downstream of the cowl exit plane as compared to the straight configuration. From Mach 2 to 3 (figs. 29(b) to (d)), the centerline pressures remained slightly below ambient (in a drag condition), and distributions showed that the straight ramp had less cowl exit-plane expansion than the curved ramp. However, the two configurations agreed in pressures along the remaining length. At Mach 3.5, the pressures were all above ambient, producing positive forces along the ramp surface.

Ramp Curvature - Long Ramps

The long curved $17^\circ/8^\circ$ ramp (11° chordal angle) was compared to the long straight 11° ramp. Both configurations had an internal expansion ratio of 1.25 and long rectangular sidewalls (fig. 7(a)).

Internal performance.—At static conditions, the performance comparison of the long ramps only slightly resembled that of their short counterparts. The extended cowl, used with both ramps for this comparison, extended past the nozzle-connect station. It influenced ramp pressure distributions by inhibiting the initial expansion at the beginning of the ramp. Therefore, the long ramps were not expected to produce results identical to those of the short ramps. At pressure ratios above 4.5, the long curved ramp generated more thrust than the long straight ramp (fig. 30(a)). The two performance curves peaked near the same NPR, but the thrust of the long straight ramp decreased more rapidly with NPR than the curved ramp, and its final level was significantly lower.

The static thrust vector angle plot (fig. 30(b)) showed that the long straight ramp swept through a larger range of values than the long curved ramp. The curved ramp's thrust vector angle increased slightly with NPR at first, then steadied out at an angle near -8° (its trailing edge angle). The same reasoning applied for the thrust vector angle variation of the short ramps is also applicable for the long ramps: at low NPR's, the curved ramp had a smaller negative normal force caused by an aft surface recompression resulting in a smaller negative thrust vector angle; at high NPR's, the straight ramp had a more symmetric flowfield in the axial direction, resulting in a smaller normal force and a smaller negative thrust vector angle.

Installed performance.—At wind-on conditions (last four points in the table II trajectory), the long ramp curvature comparison was similar to the short ramp comparison. Again, the straight ramp was not tested at Mach 3 and 3.5 because of facility and scheduling delays.

The net thrust of the straight ramp was visibly lower than the long ramp for the two lower Mach number conditions (fig. 31(a)). The drag of the two ramps was nearly equal (fig. 31(b)). As with the two short ramps, the same arguments apply to the two long ramps.

The lift ratio (fig. 31(c)) showed a slightly different result between the long ramp comparison and the short ramp comparison. At the two lower Mach numbers, the negative normal force generated by the long straight ramp was less than that of the long curved ramp. An explanation for this was found in the ramp pressure distributions (fig. 32(b) to (e)). Initially along the expansion surface, the centerline pressures on the straight ramp were not as low as those on the curved ramp. The higher initial surface pressure caused a lower overall negative normal force on the straight ramp, which was reflected in the lift ratio plot.

Ramp surface pressures.—Ramp centerline pressure distributions for the two long ramps are shown in figures 32(a) to 32(e). As discussed in the previous section the curved ramp's lower initial surface pressures were the result of a larger initial expansion (turning angle).

Ramp Length

A comparison of ramp length was made with the two curved ramps—the short curved 25°/6° ramp and the long curved 17°/8° ramp. The geometries are shown in figures 5(a) and (c). The short ramp was 15.021 in. in length and the long ramp was 21.278 in. Both configurations included short sidewalls and short cowl 1 ($\epsilon_1 = 1.0$).

Internal performance.—The internal performance parameters are shown in figures 33(a) and (b). The thrust of the long ramp was about 3 to 4 percent higher than that of the short ramp at static conditions (fig. 33(a)). Although the two geometries showed a large difference in thrust level, their static thrust vector angle curves (fig. 33(b)) showed similar trends. At low NPR's, the angle value was close to that of the ramp trailing edge angle. As NPR increased, it neared a value of zero, demonstrating that the jet flowfield became more symmetric at higher pressures.

Installed performance.—At installed conditions (last four points of table II trajectory), the two geometries again showed similar trends in performance. There was a noticeable difference only in the net thrust ratio: the long ramp achieved values about 2 to 3 percent higher than the short ramp (fig. 34(a)). The drag coefficient (fig. 34(b)) and lift ratio (fig. 34(c)) were in very close agreement between configurations at the specific Mach number and NPR conditions.

Ramp surface pressures.—The ramp pressure distributions for the points in the trajectory are shown in figure 35. At static conditions (fig. 35(a)), the long ramp showed a slightly higher upstream internal pressure and a larger initial expansion than the short ramp. At installed conditions (figs. 35(b) to (e)), the slightly higher internal pressure was still evident, but the initial expansion and downstream ramp surface pressures were similar for the two ramp geometries. The higher internal pressure, resulting from a slight difference in internal upstream contour between the two configurations, was presumably the cause of the higher thrust values achieved by the long ramp.

CONCLUSIONS

Several different single expansion ramp hypersonic nozzle configurations were tested in the NASA Lewis 10-Foot by 10-Foot Supersonic Wind Tunnel as a continuation of a previous test in the NASA

Langley 16-Foot Transonic Wind Tunnel. The effect of changing major geometry variables was studied by interchanging model expansion ramp, sidewall, and cowl hardware. The geometry variables included sidewall length and shape, cowl length, shape, and boattail angle, and ramp length and curvature. The configurations were tested at Mach numbers of 0, 2.0, 2.5, 3.0, and 3.5 and nozzle pressure ratios up to 190, although data is presented only for pressure ratios up to 35.

The test conditions were off-design, at low supersonic speeds instead of hypersonic speeds, and the nozzle configurations were expected to perform poorly as a result of their highly overexpanded flowfields in this speed regime. The main objective of the test was to extend the speed range of the database previously generated by Langley for the same nozzle configurations.

A small discrepancy in discharge coefficient and thrust ratio was found at static conditions between the Langley data and the Lewis data. This result was justified by the fact that two different flow-measuring techniques were used in the data reduction, and the jet exit simulation rig and force balance were disassembled between the two tests (which took place in two different facilities).

Model test configuration hardware consisted of four different expansion ramps, four different sets of sidewalls, and seven different cowls. The four expansion ramps had the following geometries: long curved ramp with a 17° initial angle and 8° trailing-edge angle, short curved ramp with a 25° initial angle and 6° trailing-edge angle, long straight 11° ramp, and short straight 16° ramp. Two matching sidewalls (a set) were installed for each configuration: two sets of rectangular sidewalls terminating at both short and long cowl trailing edges and two sets of triangular sidewalls extending to partial length and full length of the expansion ramp. The cowl geometries consisted of four short cowls with internal expansion ratios of 1.0, 1.1, 1.2, and 1.3 and three long cowls of internal expansion ratios 1.0, 1.25, and 1.5.

Configurations were compared both at static (wind-off) and installed (wind-on) conditions along a typical hypersonic vehicle trajectory, and the following conclusions and trends were observed:

1. Generally, at transonic and low supersonic speeds along a projected flight trajectory, the hypersonic SERN nozzles under investigation demonstrated very low performance (low thrust, high drag) overall.
2. Short sidewalls, terminating at the cowl trailing edge, performed slightly better than partial and full triangular sidewalls, which extended along the sides of the expansion ramp.
3. Changes in sidewall configuration had almost no effect on the nozzle ramp surface pressures either along the centerline or close to the edge.
4. Static and installed thrust performance improved slightly as internal expansion ratio increased.
5. A long cowl delayed overexpansion of the flow at the start of the nozzle expansion ramp. It produced thrust levels approximately 1 to 2 percent higher than the short cowls by maintaining higher pressures at the forward part of the ramp where the projected area is largest for axial force.
6. A large cowl boattail angle increased drag, therefore reducing net thrust (thrust-minus-drag) by 3 to 4 percent. Its upturned contour delayed the initial overexpansion, a result similar to that of the long cowl.

7. At installed conditions, curved ramps generated higher thrust than straight ramps while their drag levels remained approximately equal.

8. At both static and installed conditions, the long curved ramp generated higher thrust than the short curved ramp.

APPENDIX—NOMENCLATURE/SYMBOLS

A_{exit}	exit area of ducted nozzle, in. ²
A_{ref}	largest upstream model area, in. ²
A_t	nozzle throat area, in. ²
C_D	thrust-removed drag coefficient, $D/q_0 A_{\text{ref}}$, lb _f
C_d	nozzle discharge coefficient, W_P/W_I
C_p	ramp surface static pressure coefficient, $(p - p_0)/q_0$
D	nozzle thrust-removed drag, lb _f
F	measured nozzle axial force (thrust along axis), lb _f
F_G	nozzle resultant gross thrust, $\sqrt{F^2 + N^2}$, lb _f
F_I	ideal nozzle thrust, lb _f
	$W_P = \sqrt{\frac{R_j T_{t,j}}{g_c} \left(\frac{2\gamma_j}{\gamma_j - 1} \right) \left[1 - \left(\frac{1}{P_{t,j}} \right)^{(\gamma_j - 1)/\gamma_j} \right]}$
g_c	gravitational constant, 32.174 ft-lb _m /lb _f -sec ²
L	measured nozzle lift, lb _f
l	expansion ramp length (axial distance from nozzle-connect station to trailing edge), in.
M_0	tunnel freestream Mach number
N	measured nozzle normal force, lb _f
NPR	nozzle pressure ratio, $p_{t,j}/p_0$
$p_{t,j}$	jet total pressure, psi
$p_{t,0}$	tunnel freestream total pressure, psf
p	ramp surface static pressure, psi
p_0	tunnel freestream static pressure, psi
q_0	tunnel freestream dynamic pressure, psi
R_j	jet specific gas constant, 53.364 ft-lb _f /lb _m -°R for air
SERN	single expansion ramp nozzle
SSTO	single stage to orbit
$T_{t,j}$	jet total temperature, °R
W_I	ideal nozzle weight flow based on $p_{t,j}$ and $T_{t,j}$, lb _m /sec
W_P	predicted (measured) nozzle weight flow, lb _m /sec

w	expansion ramp width (not including sidewalls), in.
x	axial distance from nozzle connect station, in.
y	lateral distance outward from ramp centerline, in.
γ_j	jet specific heat ratio, 1.3997 for air
δ	thrust vector angle, $\tan^{-1}(N/F)$, deg
ε_i	internal expansion ratio, A_{exit}/A_t

REFERENCES

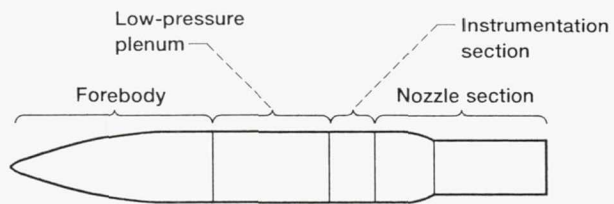
1. Leavitt, L.D.; and Lamb, M.: Transonic Characteristics of NASP Nozzles. Proceedings of 5th National Aerospace Plane Symposium, Oct. 1988, Paper No. L-7005.
2. Shyne, R.J.; and Carboni, J.D.: Experimental Investigation of Hypersonic Exhaust Nozzles at Supersonic Conditions. Proceedings of the 7th National Aerospace Plane Symposium, Oct. 1989, Paper No. 81.
3. Aiello, R.A.: NASA Lewis 10- by 10-Foot Supersonic Wind Tunnel. NASA TM X-71625, 1974.
4. Mercer, C.E., et al.: Computations for the Langley 16-Foot Transonic Tunnel-NASA, Langley Research Center, Revision 1. NASA TM-86319-REV-1, 1987.
5. Shapiro, A.H.: The Dynamics and Thermodynamics of Compressible Fluid Flow, Vol. I. Ronald Press Co., c.1953.

TABLE I. - TEST CONFIGURATION MATRIX

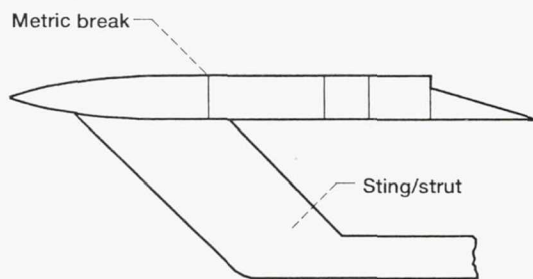
Configuration number	Ramp	Sidewalls	Cowl	A_{t_1} in. ²	ϵ_i
1	Long curved 17°/8°	Short rectangular	Short cowl 3	8.067	1.2
2	Long curved 17°/8°	Partial triangular	Short cowl 3	8.066	1.2
3	Long curved 17°/8°	Full triangular	Short cowl 3	8.052	1.2
4	Long curved 17°/8°	Short rectangular	Short cowl 1	7.940	1.0
5	Long curved 17°/8°	Short rectangular	Short cowl 2	8.064	1.1
6	Long curved 17°/8°	Short rectangular	Short cowl 4	8.103	1.3
7	Long curved 17°/8°	Long rectangular	Extended cowl	7.977	1.25
8	Long curved 17°/8°	Long rectangular	Long straight	9.410	1.5
9	Long curved 17°/8°	Long rectangular	Long upturned	8.116	1.0
10	Short curved 25°/6°	Short rectangular	Short cowl 3	8.126	1.0
11	Short straight 16°	Short rectangular	Short cowl 3	8.026	1.0
12	Long straight 11°	Long rectangular	Extended cowl	7.985	1.25

TABLE II. - TYPICAL TRAJECTORY
OF A HYPERSONIC VEHICLE

Mach number	Nozzle pressure ratio
0.00	2.0
0.60	2.0
0.80	2.5
0.90	3.0
0.95	3.5
1.20	4.0
2.00	10.0
2.50	15.0
3.00	20.0
3.50	35.0

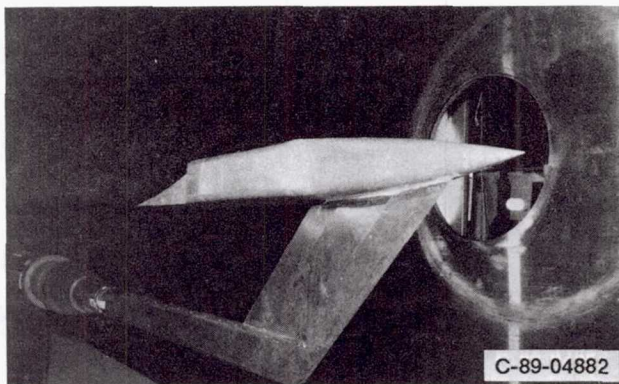


(a) Top view.

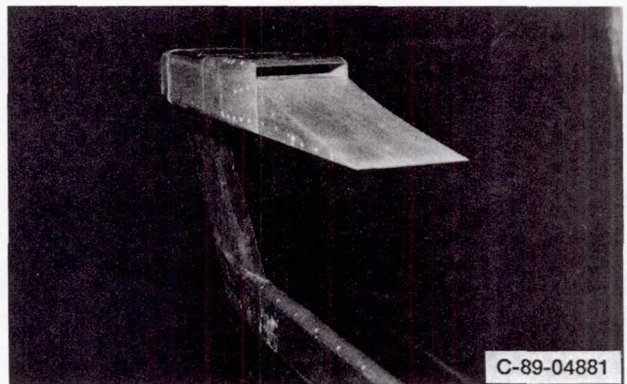


(b) Side view.

Figure 1.—Sketch of isolated afterbody/nozzle model.



(a) Front view.



(b) Rear view.

Figure 2.—Photographs of rig mounted in Lewis 10x10 SWT.

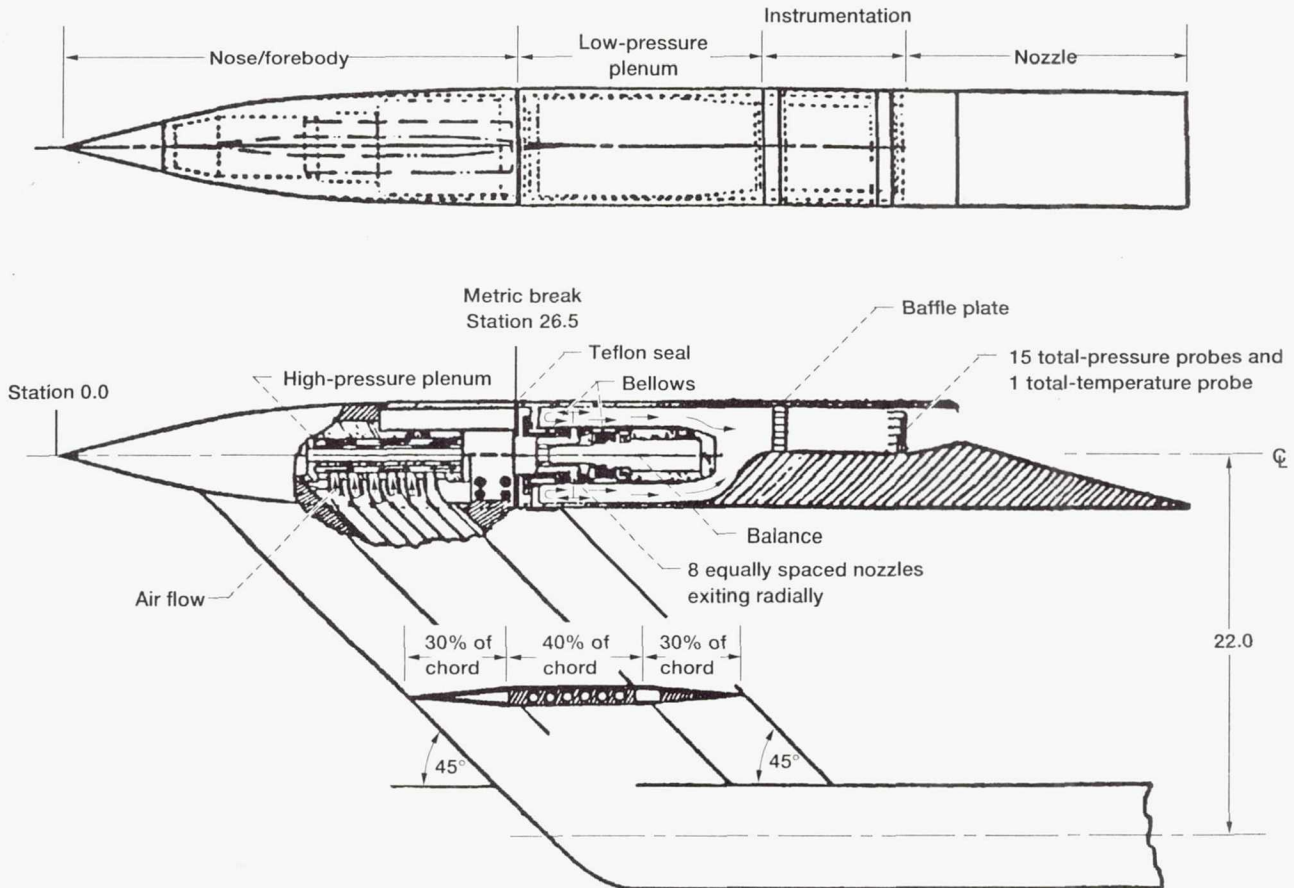


Figure 3.—Schematic of jet exhaust simulation test rig with 2-dimensional hypersonic nozzle installed (dimensions in in.).

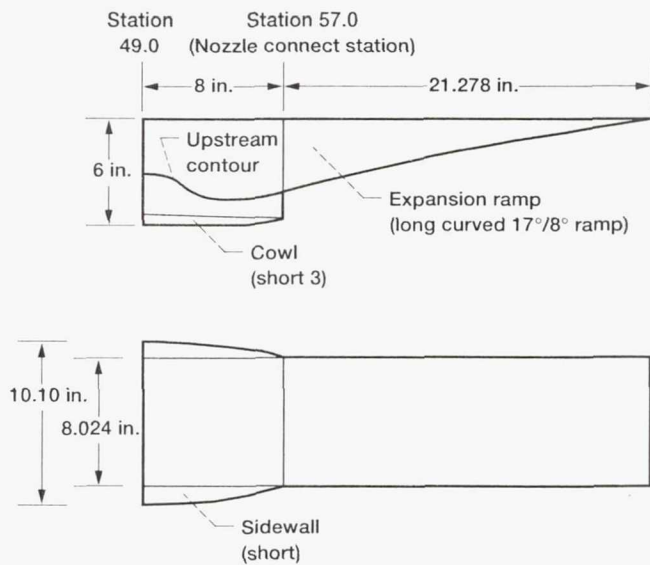
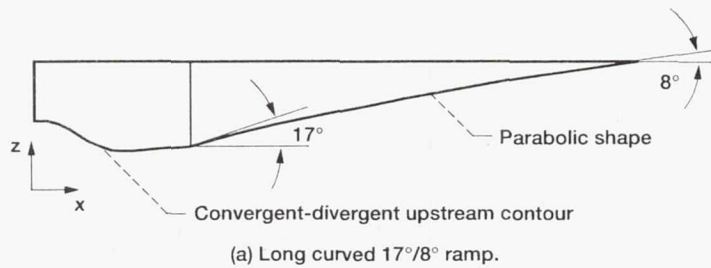
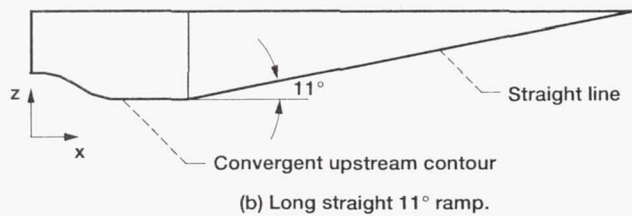


Figure 4.—Baseline configuration and arrangement of nozzle components.



Coordinates for long curved 17°/8° ramp

x	z	x	z	x	z
7.297	0.692	15.210	2.655	22.637	4.048
8.295	0.984	15.710	2.758	23.132	4.131
8.782	1.124	16.204	2.858	23.627	4.264
9.276	1.259	16.699	2.985	24.122	4.296
9.771	1.390	17.194	3.055	24.617	4.378
10.266	1.518	17.689	3.152	25.122	4.458
10.761	1.643	18.184	3.246	25.606	4.538
11.256	1.765	18.697	3.340	26.101	4.616
11.751	1.884	19.173	3.432	26.596	4.694
12.246	2.001	19.668	3.524	27.091	4.772
12.740	2.115	20.163	3.614	27.586	4.848
13.235	2.227	20.658	3.702	28.081	4.924
13.730	2.337	21.153	3.790	28.575	4.990
14.225	2.445	21.648	3.877		

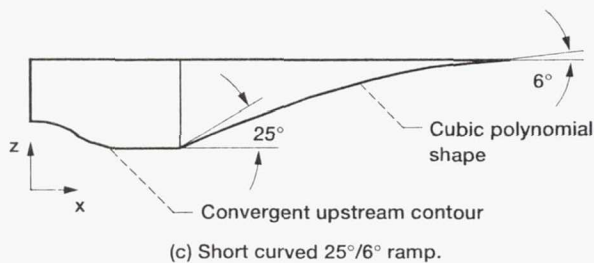


Coordinates for convergent-divergent upstream contour

x	z
0.000	2.000
0.327	1.985
0.842	1.896
1.338	1.731
1.803	1.492
2.307	1.132
2.815	0.835
3.302	0.647
3.812	0.534
4.335	0.500
4.530	0.508
7.297	0.692

Coordinates for convergent upstream contour

x	z	x	z
0.000	2.000	2.340	1.346
0.225	1.993	2.537	1.226
0.449	1.974	2.740	1.118
0.671	1.941	2.948	1.021
0.891	1.896	3.161	0.936
1.108	1.838	3.377	0.864
1.321	1.767	3.579	0.804
1.530	1.684	3.819	0.756
1.734	1.589	4.043	0.722
1.932	1.482	4.267	0.701
2.150	1.346	7.297	0.692



Coordinates for short curved 25°/6° ramp

x	z	x	z	x	z
7.297	0.692	12.797	2.881	18.297	4.347
7.797	0.921	13.297	3.045	18.797	4.444
8.297	1.143	13.797	3.202	19.297	4.535
8.797	1.360	14.297	3.353	19.797	4.619
9.297	1.571	14.797	3.498	20.297	4.698
9.797	1.776	15.297	3.638	20.797	4.771
10.297	1.975	15.797	3.771	21.297	4.837
10.797	2.168	16.297	3.898	21.797	4.898
11.297	2.356	16.797	4.019	22.297	4.952
11.797	2.537	17.297	4.134	22.321	4.990
12.297	2.712	17.797	4.244		

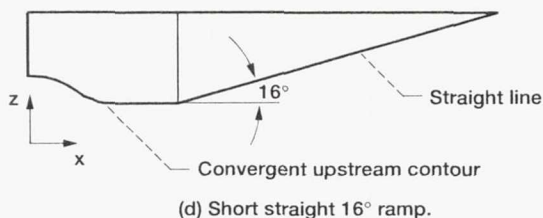
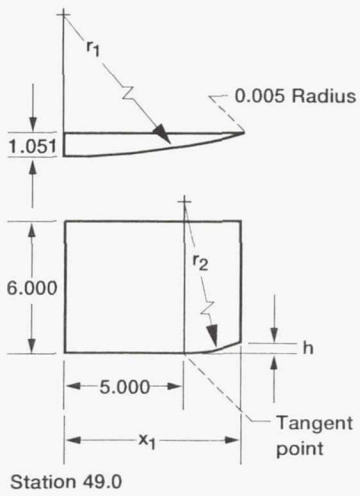
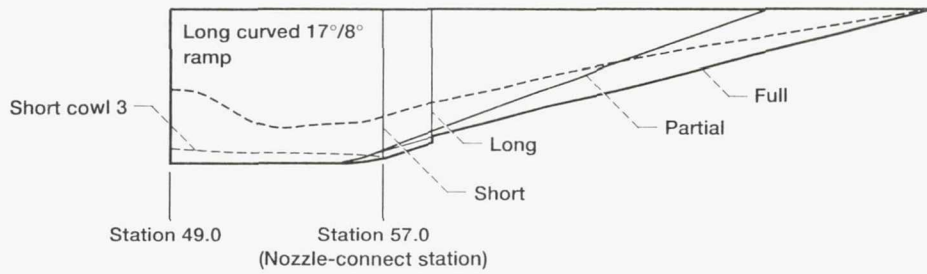
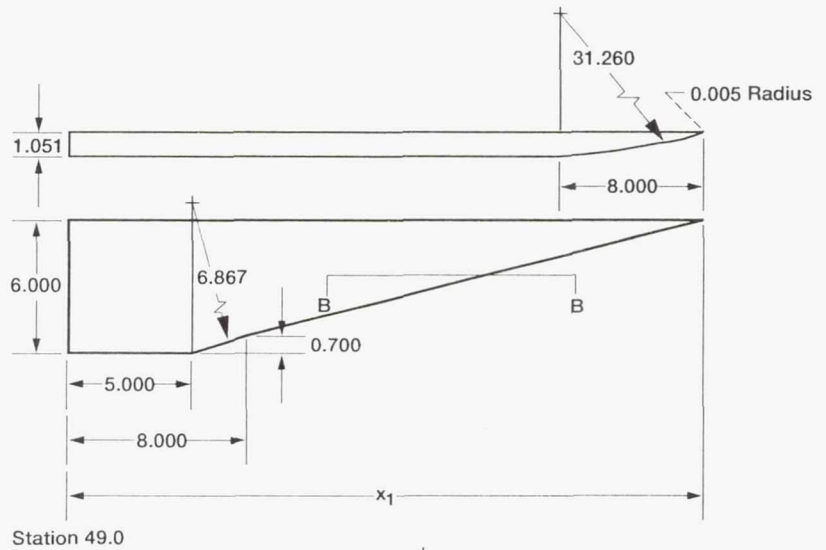


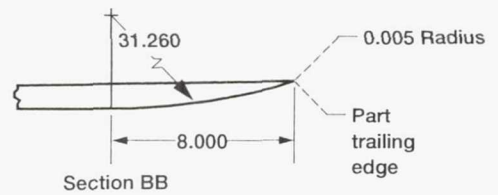
Figure 5.—Expansion ramp geometries.



Station 49.0



Station 49.0



Section BB

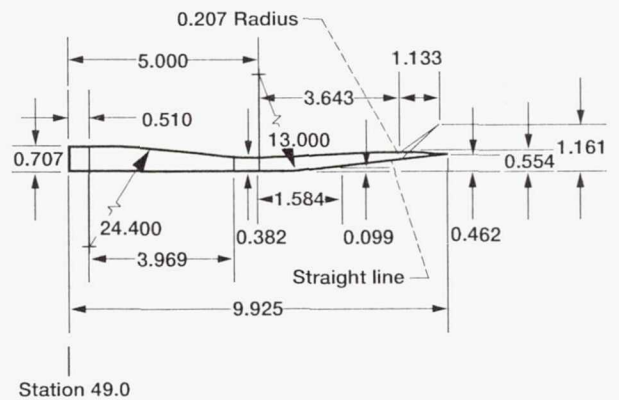
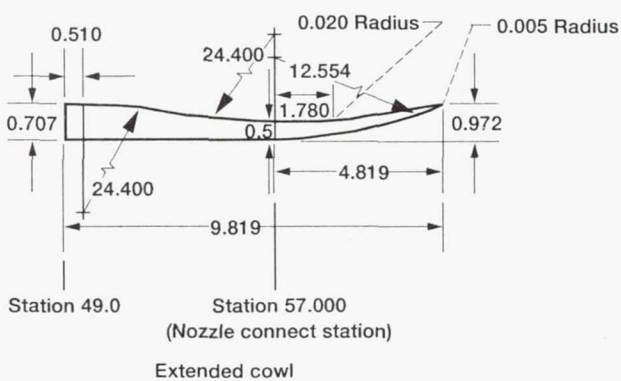
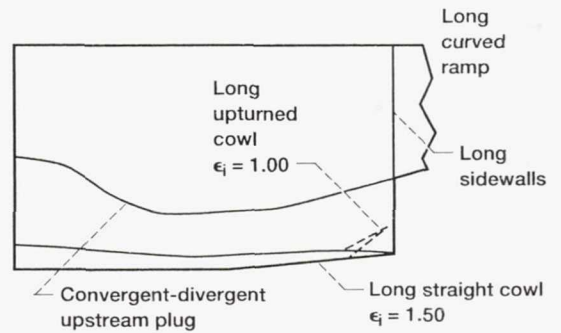
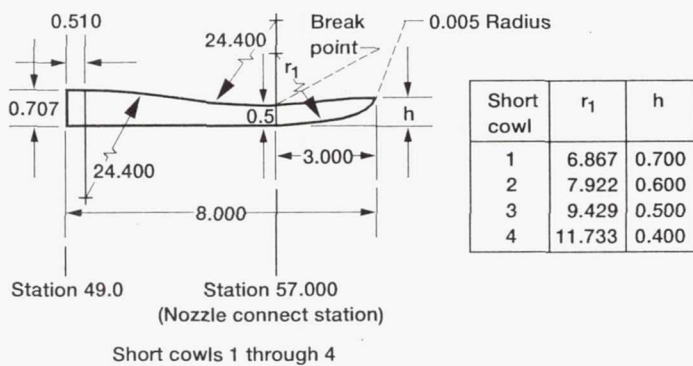
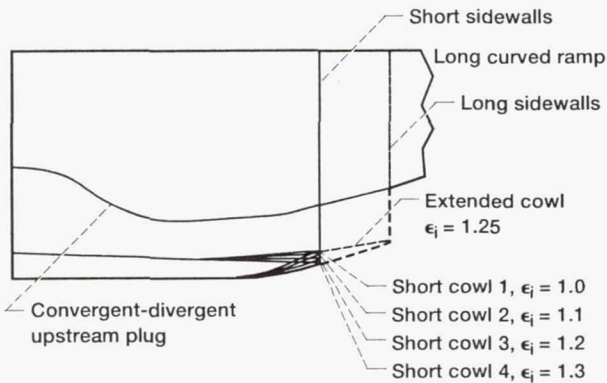
Rectangular sidewalls

Sidewall	x_1	r_1	r_2	h
Short	8.000	31.260	9.429	0.500
Long	9.819	46.819	12.554	0.972

Triangular sidewalls

Sidewall	x_1
Partial	23.024
Full	29.278

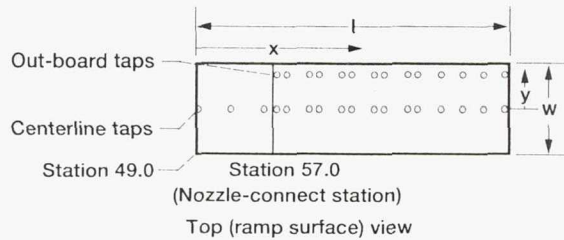
Figure 6.—Sidewall geometries.



(a) Internal expansion ratio geometries, short and extended cowls (dimensions in in.).

(b) Cowl boattail angle geometry variations (dimensions in in.).

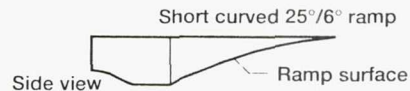
Figure 7.—Various sidewall and cowl geometries.



Pressure tap locations
 $l = 21.278$ in., $w = 8.024$ in.

	Centerline	Outboard	x/l
$y/(w/2)$	0.0000	0.7478	
1			-0.3055
2			-0.1880
3			-0.0470
4		1	0.0047
5		2	0.0470
6		3	0.1410
7		4	0.1880
8		5	0.2820
9		6	0.3290
10		7	0.4230
11		8	0.4700
12		9	0.5640
13		10	0.6110
14		11	0.7050
15		12	0.7989
16		13	0.8929
17		14	0.9869

(a) Long curved $17^\circ/8^\circ$ ramp.



Pressure tap locations
 $l = 15.021$ in., $w = 8.024$ in.

	Centerline	Outboard	x/l
$y/(w/2)$	0.0000	0.7478	
1			-0.4326
2			-0.2662
3			-0.0660
4		1	0.0660
5		2	0.1331
6		3	0.1997
7		4	0.2662
8		5	0.3328
9		6	0.3994
10		7	0.4659
11		8	0.5325
12		9	0.5990
13		10	0.6656
14		11	0.7322
15		12	0.7987
16		13	0.8653
17		14	0.9318

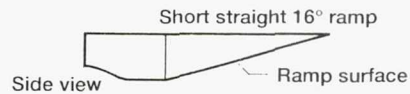
(c) Short curved $25^\circ/6^\circ$ ramp.



Pressure tap locations
 $l = 21.278$ in., $w = 8.024$ in.

	Centerline	Outboard	x/l
$y/(w/2)$	0.0000	0.7478	
1			-0.3055
2			-0.1880
3			-0.0470
4		1	0.0470
5		2	0.0940
6		3	0.1880
7		4	0.2350
8		5	0.3290
9		6	0.3760
10		7	0.4700
11		8	0.5170
12		9	0.6110
13		10	0.6580
14		11	0.7520
15		12	0.7989
16		13	0.8929
17		14	0.9869

(b) Long straight 11° ramp.



Pressure tap locations
 $l = 15.021$ in., $w = 8.024$ in.

	Centerline	Outboard	x/l
$y/(w/2)$	0.0000	0.7478	
1			-0.4326
2			-0.2662
3			-0.0660
4		1	0.0660
5		2	0.1331
6		3	0.1997
7		4	0.2662
8		5	0.3328
9		6	0.3994
10		7	0.4659
11		8	0.5325
12		9	0.5990
13		10	0.6656
14		11	0.7322
15		12	0.7987
16		13	0.8653
17		14	0.9318

(d) Short straight 16° ramp.

Figure 8.—Static pressure orifice position descriptions.

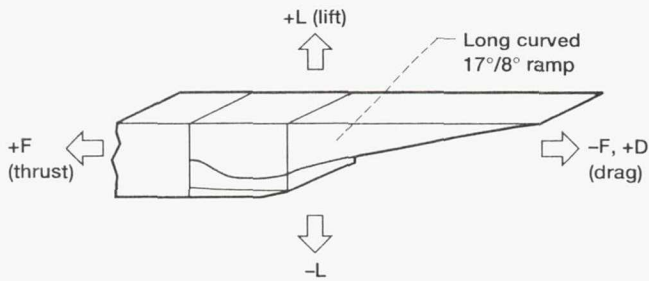


Figure 9.—Sign conventions used for nozzle forces.

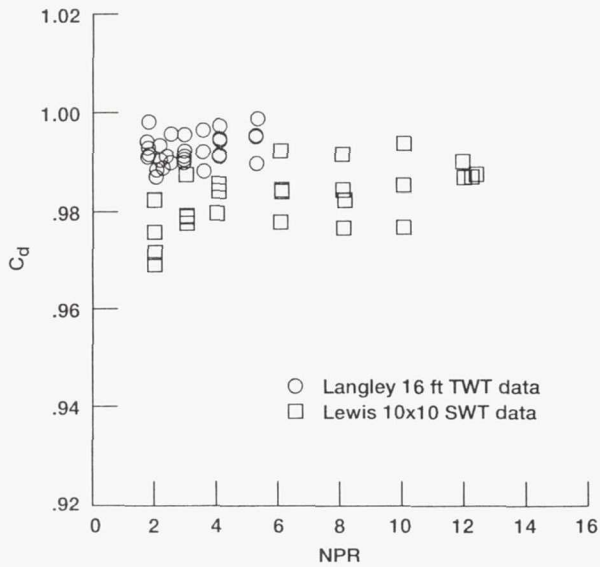


Figure 10.—Comparison of Lewis and Langley static discharge coefficient.

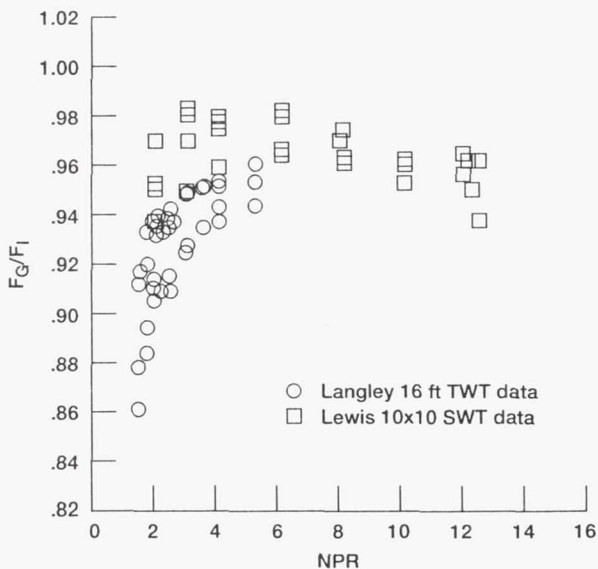


Figure 11.—Comparison of Lewis and Langley static thrust ratio.

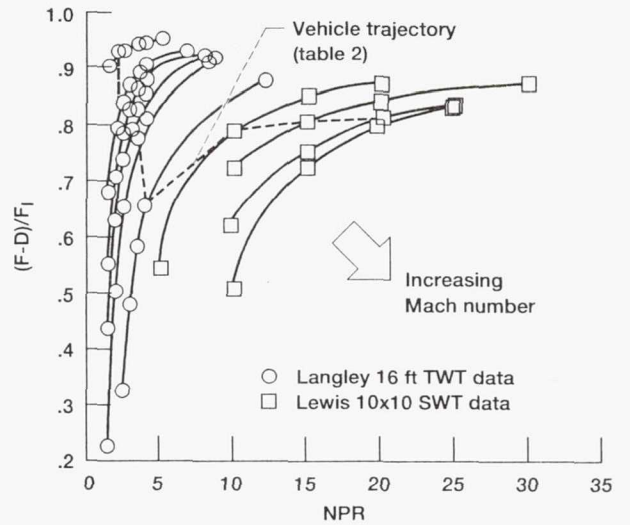
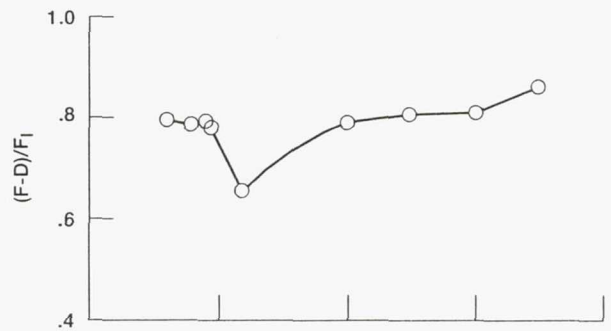
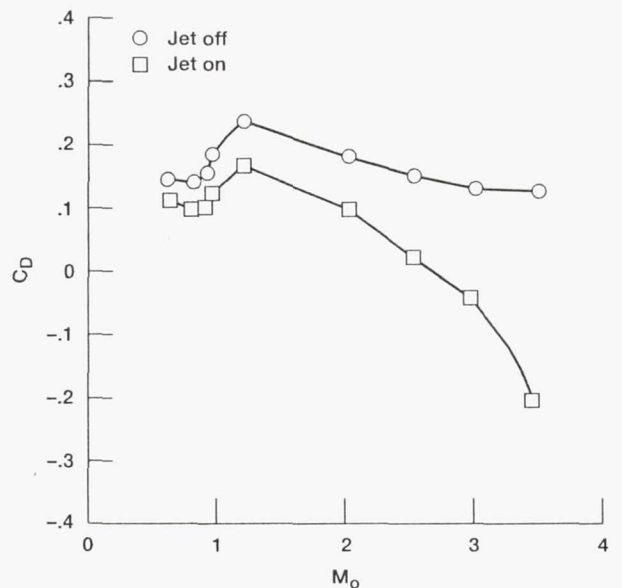


Figure 12.—Effect of Mach number on installed performance of baseline configuration (long curved 17°/8° ramp, short sidewalls, short cowl 3).

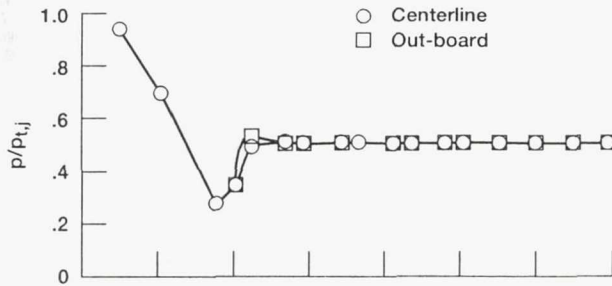


(a) Net thrust ratio at points along NPR-Mach number schedule (table 2).

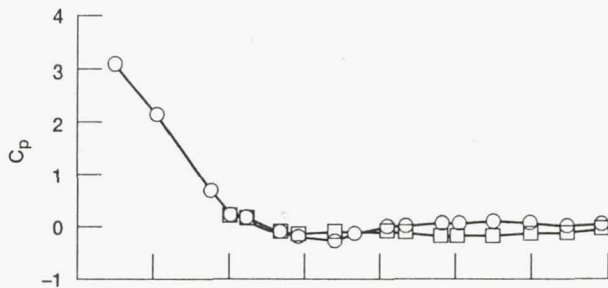


(b) Drag coefficient at points along NPR-Mach number schedule (table 2).

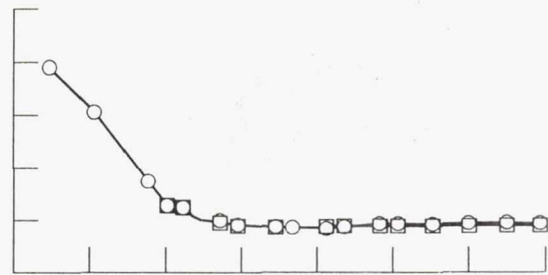
Figure 13.—Installed performance of baseline configuration (long curved 17°/8° ramp, short sidewalls, short cowl 3).



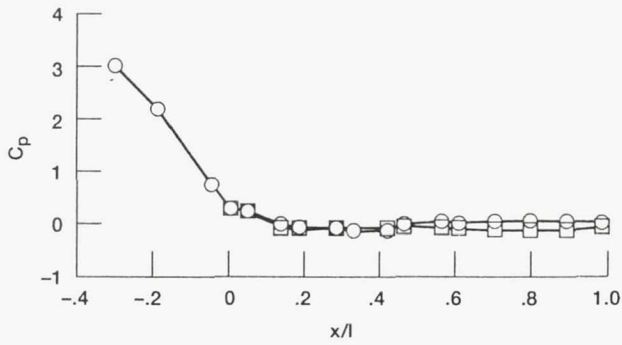
(a) (a-1) Mach number = 0.0, NPR = 2.



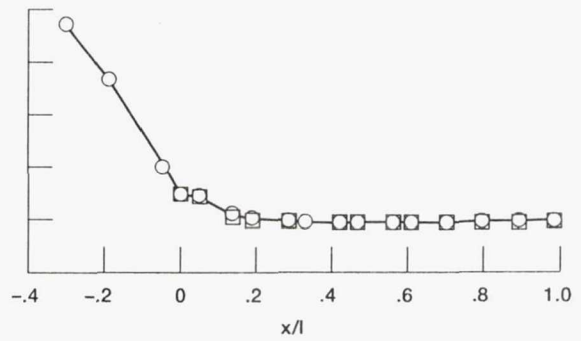
(b) (b-1) Mach number = 2.0, NPR = 10.



(d) (d-1) Mach number = 3.0, NPR = 20.

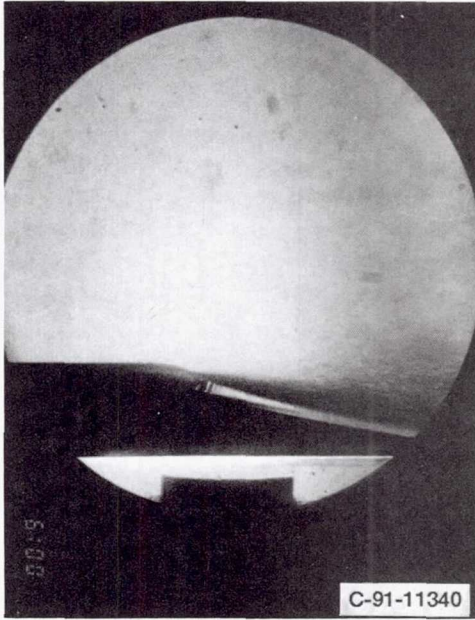


(c) Mach number = 2.5, NPR = 15.



(e) Mach number = 3.5, NPR = 35.

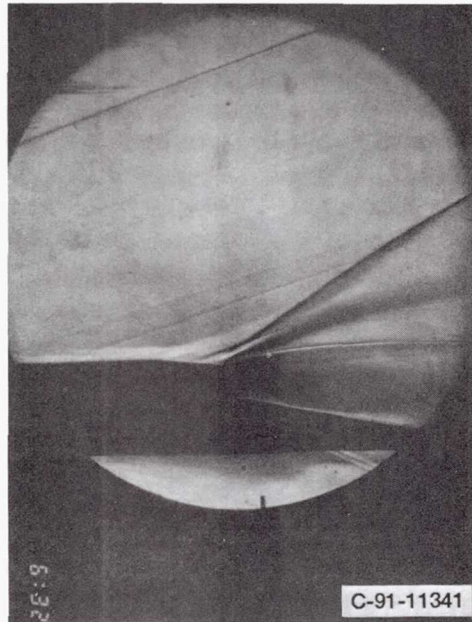
Figure 14.—Ramp pressure distributions for baseline configuration.



(a-2) Tunnel off.

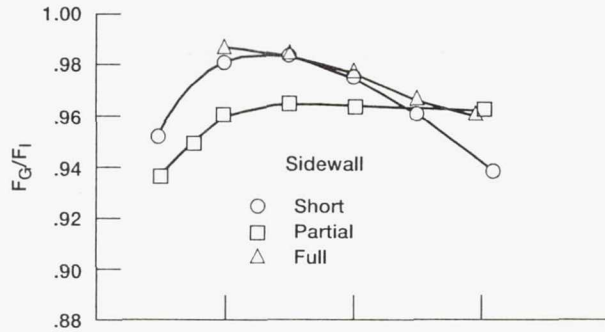


(b-2) Low NPR, low M.

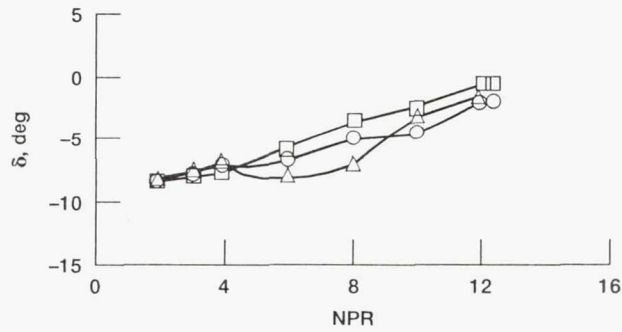


(d-2) High NPR, high M.

Figure 14.—Concluded.

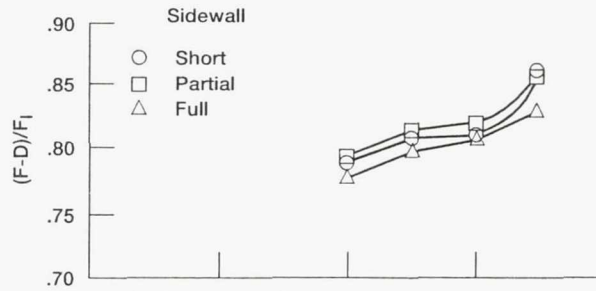


(a) Static thrust ratio.

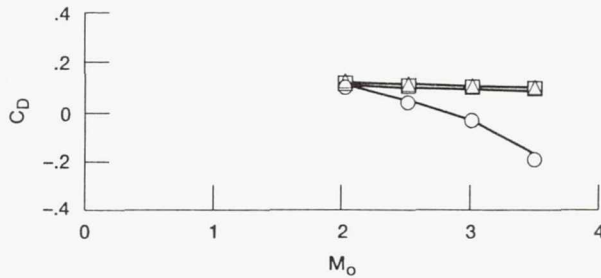


(b) Static thrust vector angle.

Figure 15.—Effect of sidewall geometry on internal performance (long curved 17°/8° ramp, short cowl 3).



(a) Net thrust ratio at trajectory points (table 2).



(b) Thrust-removed drag coefficient at trajectory points (table 2).

Figure 16.—Effect of sidewall geometry on installed performance (long curved 17°/8° ramp, short cowl 3).

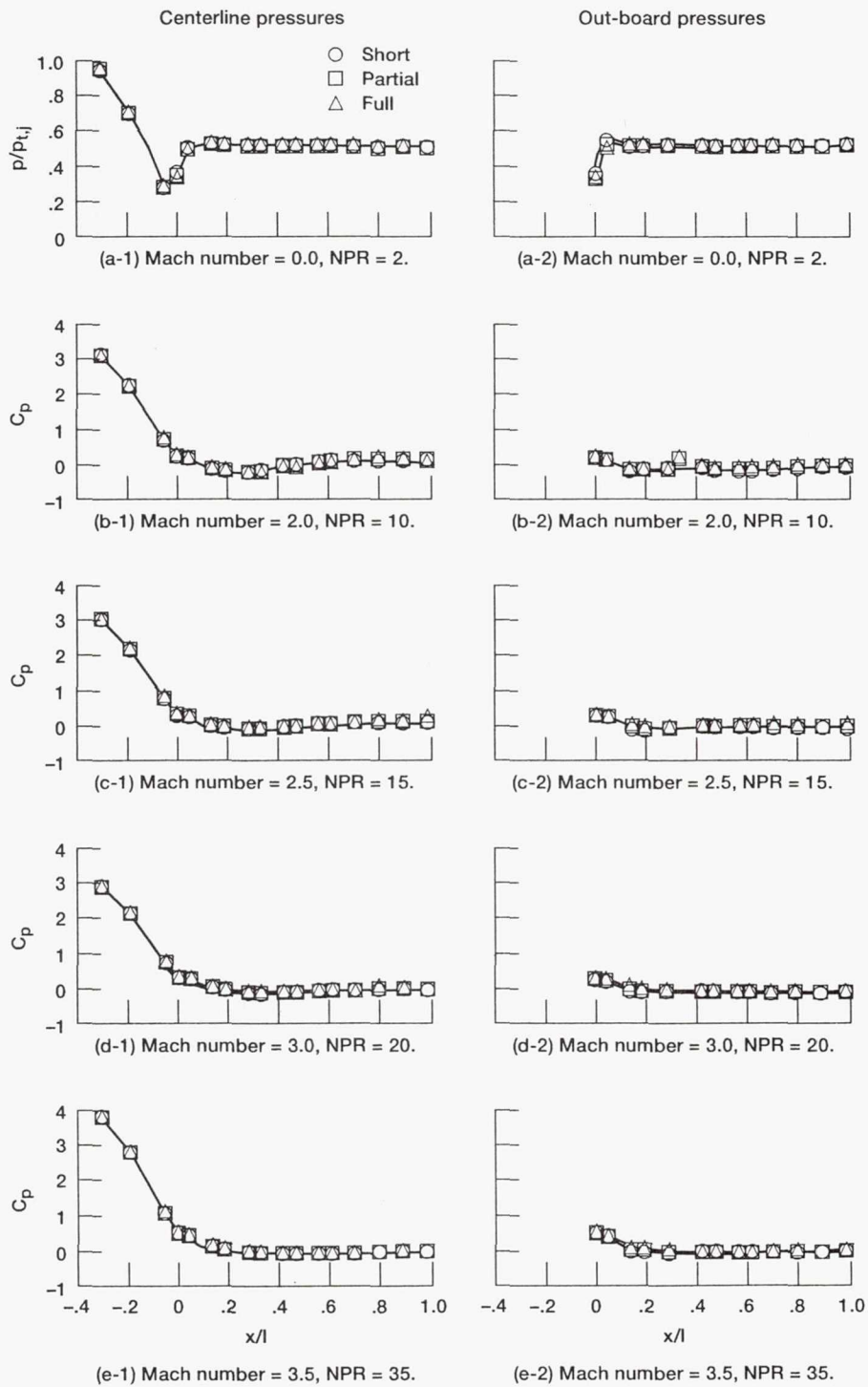
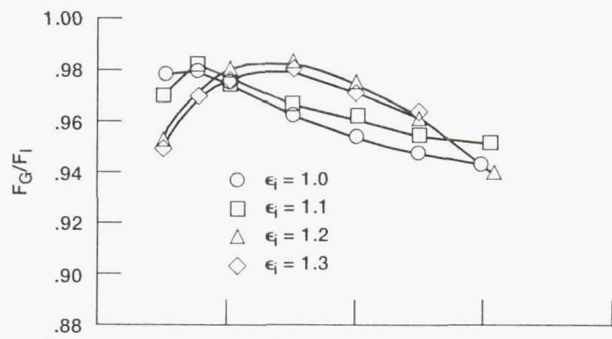
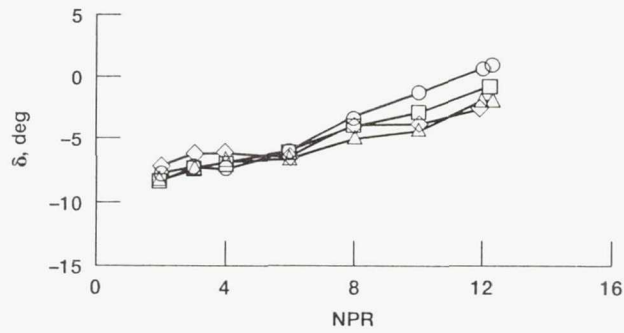


Figure 17.—Effect of sidewall geometry on ramp pressure distributions.

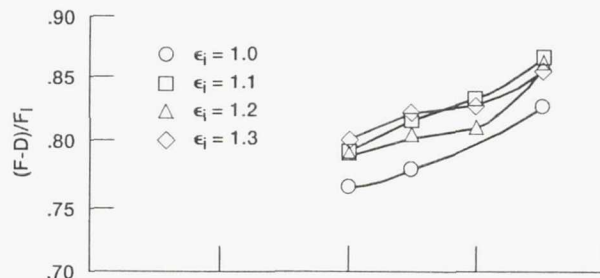


(a) Static thrust ratio.

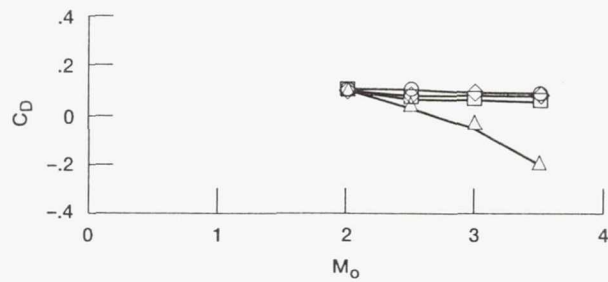


(b) Static thrust vector angle.

Figure 18.— Effect of internal expansion ratio on internal performance (long curved $17^\circ/8^\circ$ ramp with short sidewalls).

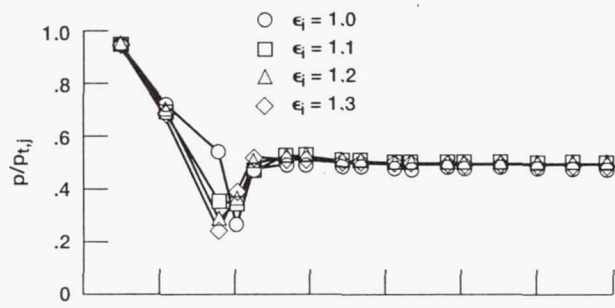


(a) Net thrust ratio at trajectory points (table 2).

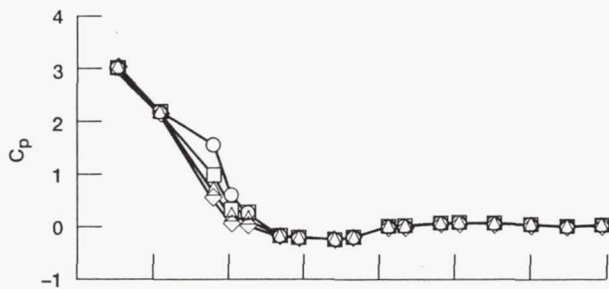


(b) Thrust-removed drag coefficient at trajectory points (table 2).

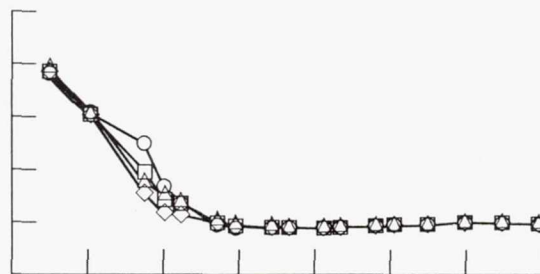
Figure 19.—Effect of internal expansion ratio on installed performance (long curved $17^\circ/8^\circ$ ramp with short sidewalls).



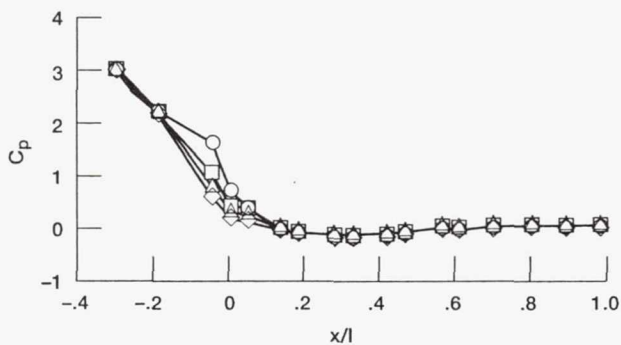
(a) Mach number = 0.0, NPR = 2.



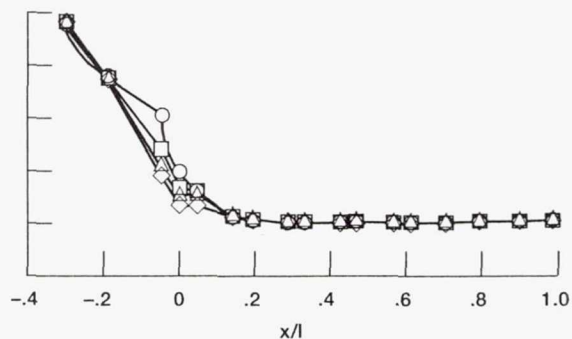
(b) Mach number = 2.0, NPR = 10.



(d) Mach number = 3.0, NPR = 20.

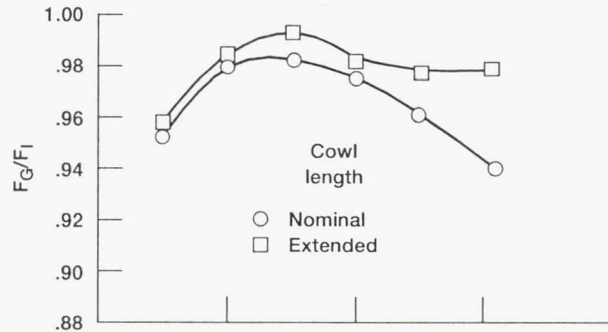


(c) Mach number = 2.5, NPR = 15.

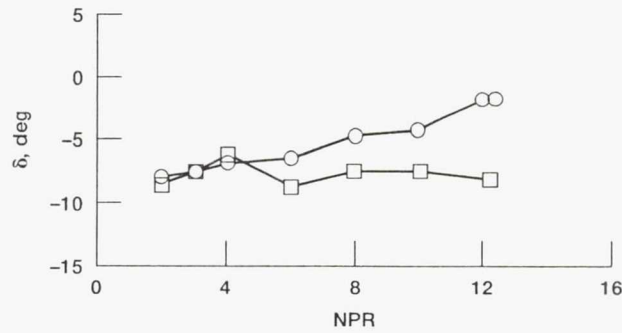


(e) Mach number = 3.5, NPR = 35.

Figure 20.—Effect of internal expansion ratio on ramp centerline pressure distributions.

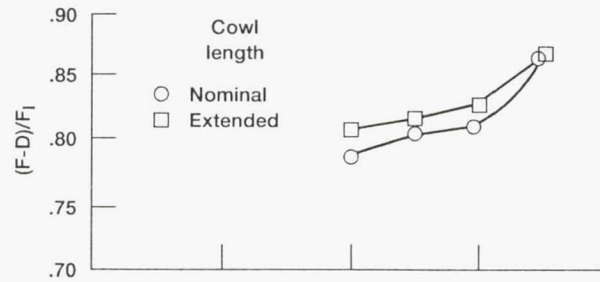


(a) Static thrust ratio.

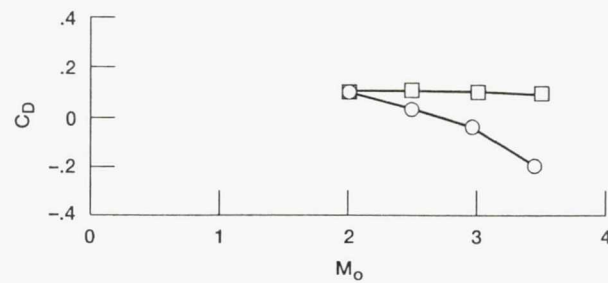


(b) Static thrust vector angle.

Figure 21.—Effect of extended cowl on internal performance (long curved 17°/8° ramp, sidewalls corresponding to cowl length).

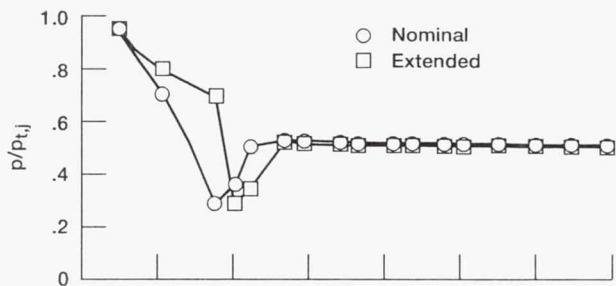


(a) Net thrust ratio at trajectory points (table 2).

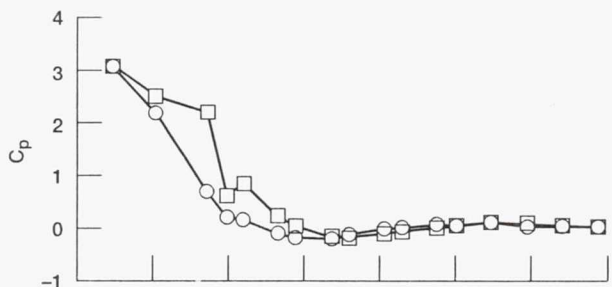


(b) Thrust-removed drag coefficient at trajectory points (table 2).

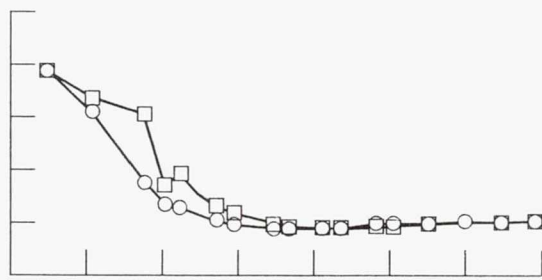
Figure 22.—Effect of extended cowl on installed performance (long curved 17°/8° ramp, sidewalls corresponding to cowl length).



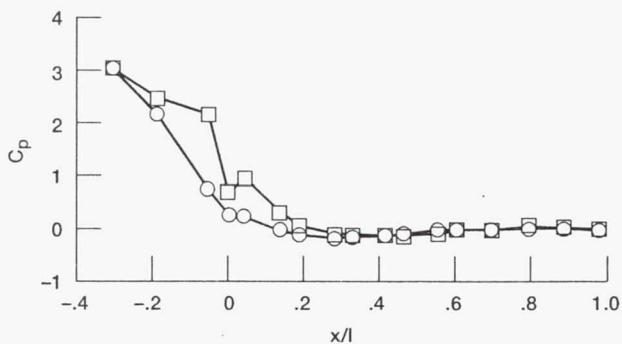
(a) Mach number = 0.0, NPR = 2.



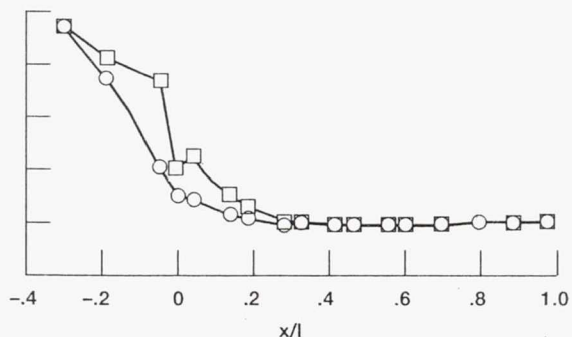
(b) Mach number = 2.0, NPR = 10.



(d) Mach number = 3.0, NPR = 20.



(c) Mach number = 2.5, NPR = 15.



(e) Mach number = 3.5, NPR = 35.

Figure 23.—Effect of extended cowl on ramp centerline pressure distributions.

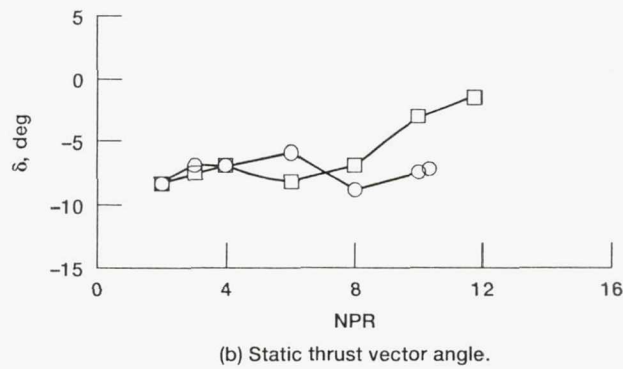
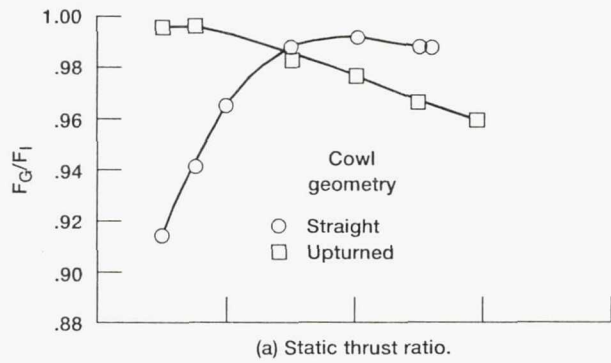


Figure 24.—Effect of boattail angle on internal performance (long curved $17^\circ/8^\circ$ ramp with long sidewalls).

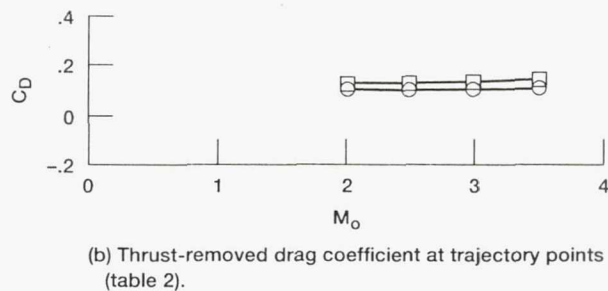
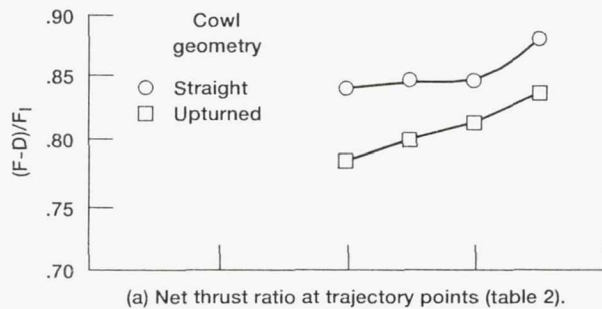


Figure 25.—Effect of boattail angle on installed performance (long curved $17^\circ/8^\circ$ ramp with long sidewalls).

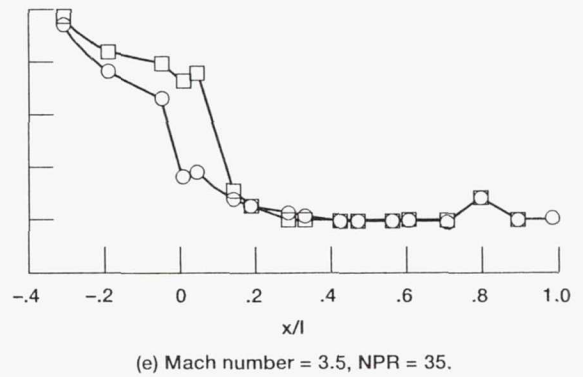
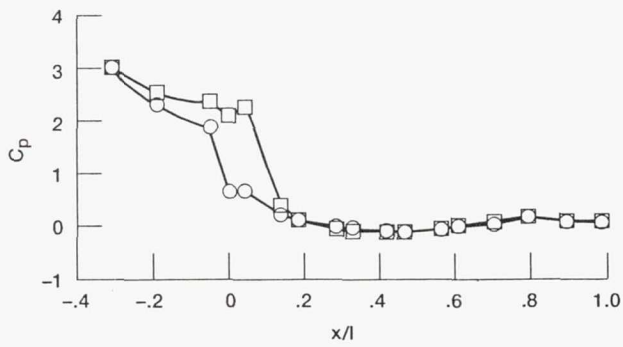
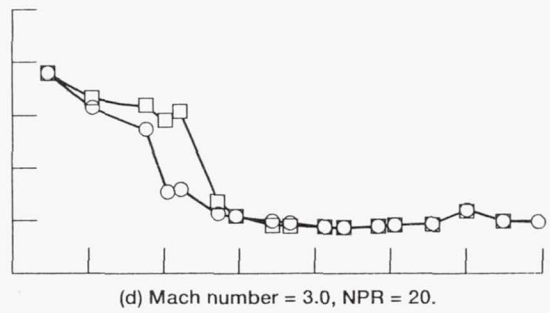
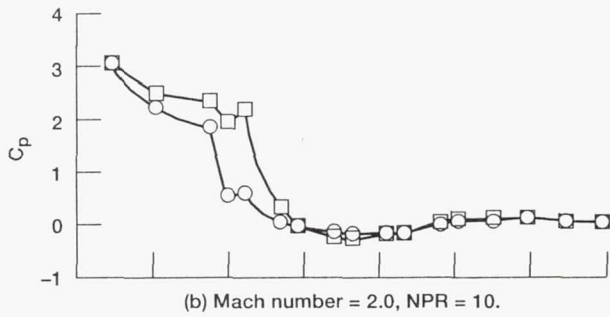
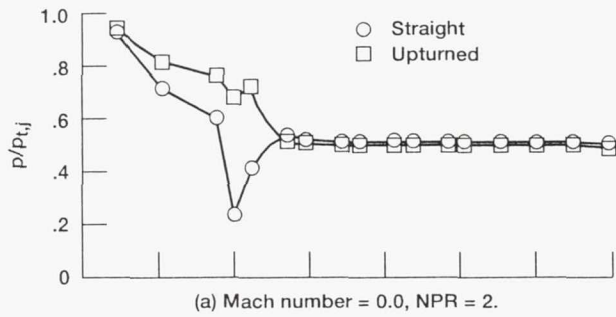
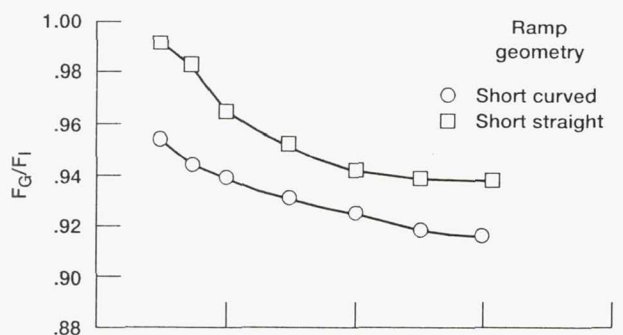
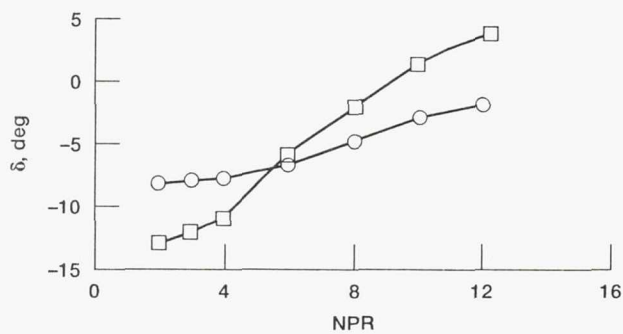


Figure 26.—Effect of boattail angle on ramp centerline pressure distributions.

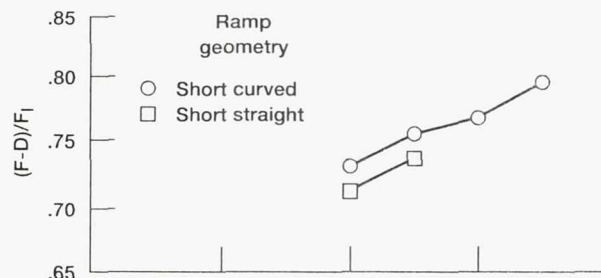


(a) Static thrust ratio.



(b) Static thrust vector angle.

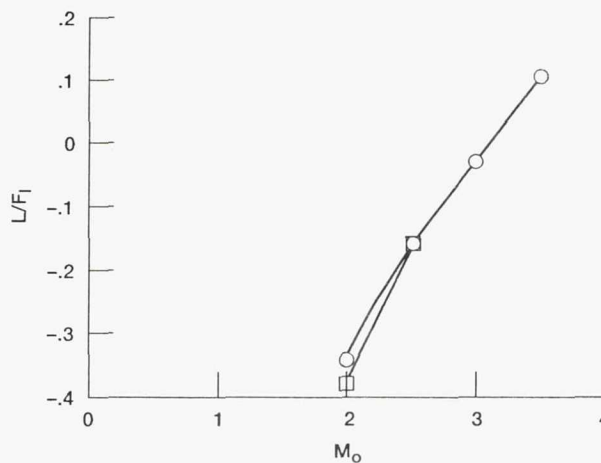
Figure 27.—Effect of ramp curvature on internal performance—short ramps ($\epsilon_1 = 1.0$, short sidewalls).



(a) Net thrust ratio at trajectory points (table 2).



(b) Thrust-removed drag coefficient at trajectory points (table 2).



(c) Lift ratio at trajectory points (table 2).

Figure 28.—Effect of ramp curvature on installed performance—short ramps ($\epsilon_1 = 1.0$, short sidewalls).

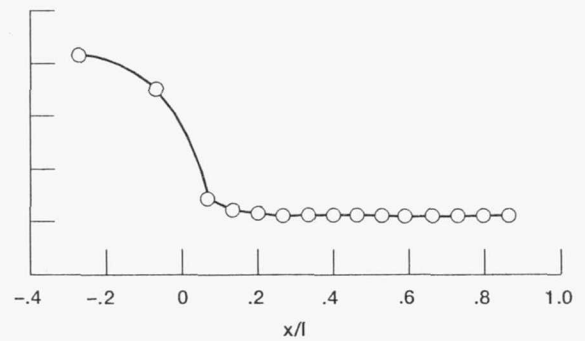
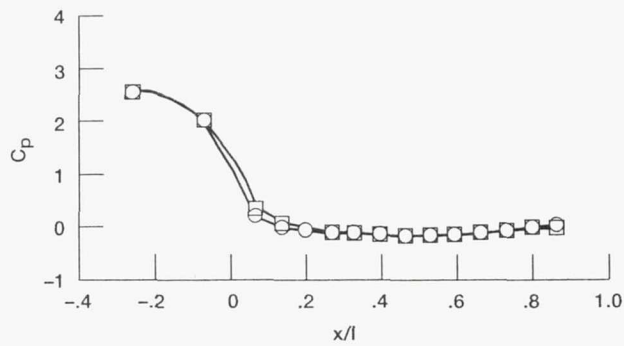
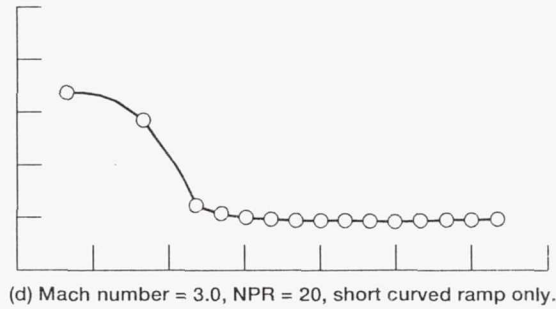
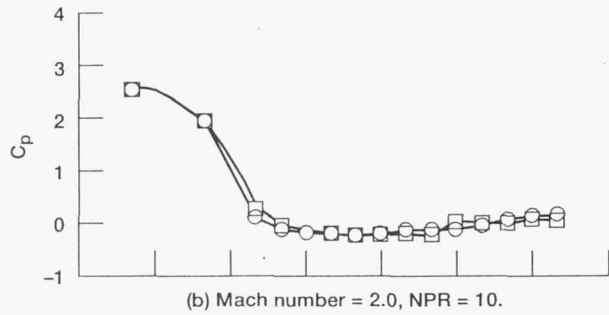
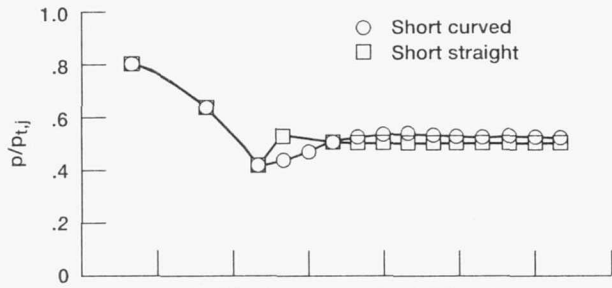


Figure 29.—Effect of ramp curvature on ramp centerline pressure distributions—short ramps.

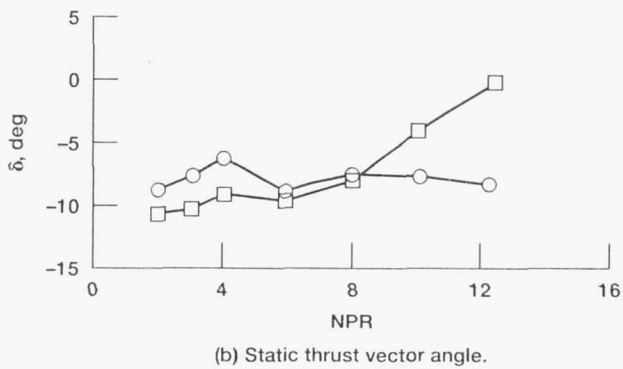
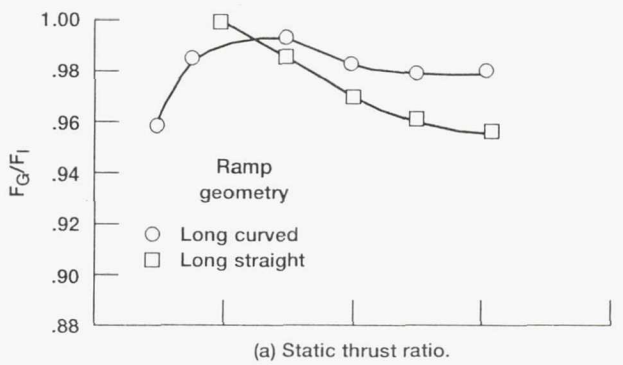


Figure 30.—Effect of ramp curvature on internal performance—long ramps ($\epsilon_i = 1.25$, long sidewalls).

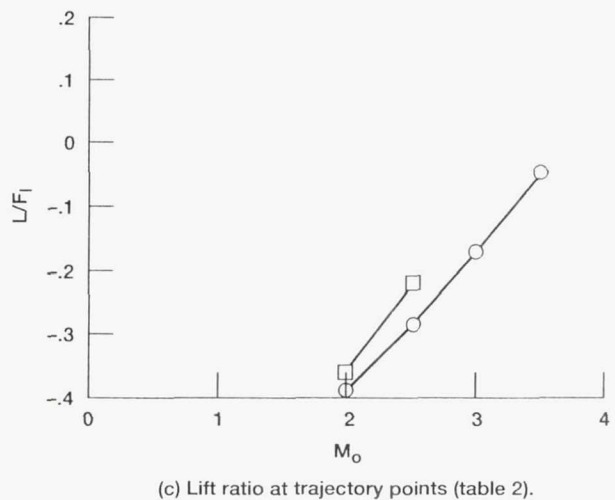
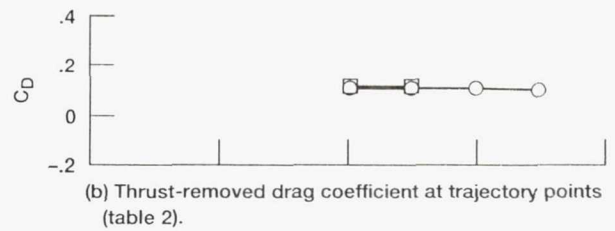
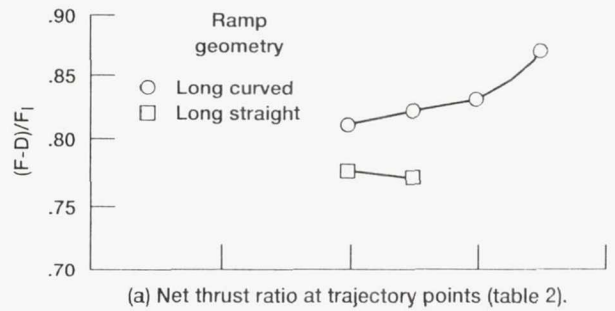


Figure 31.—Effect of ramp curvature on installed performance—long ramps ($\epsilon_i = 1.0$, long sidewalls).

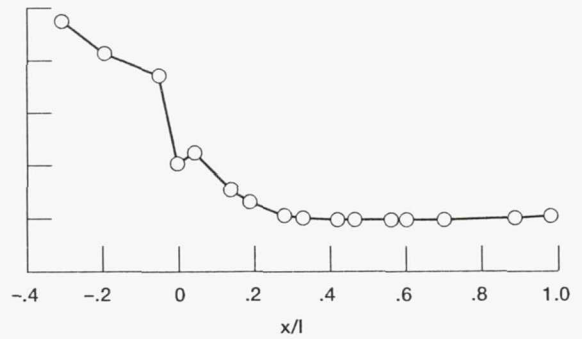
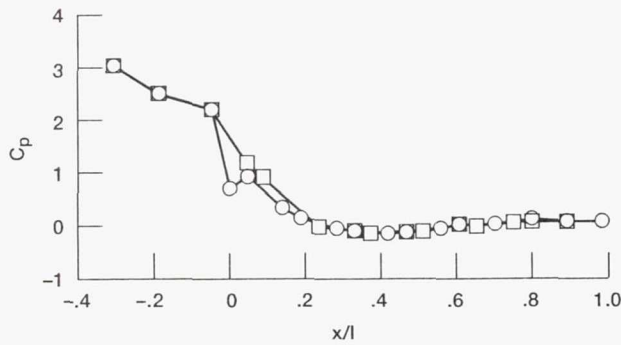
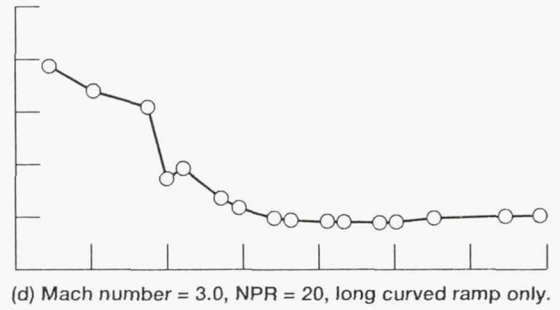
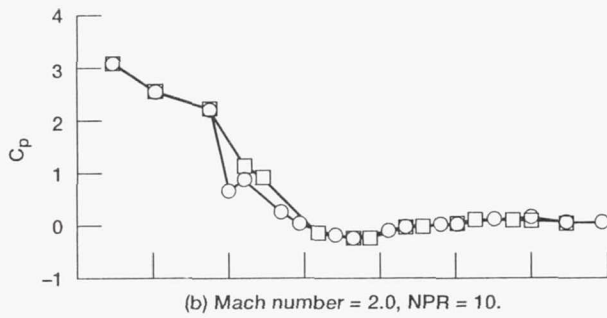
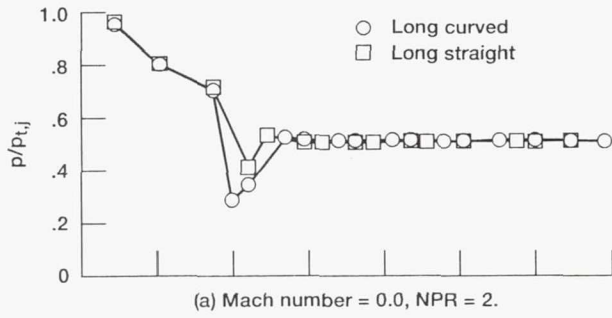
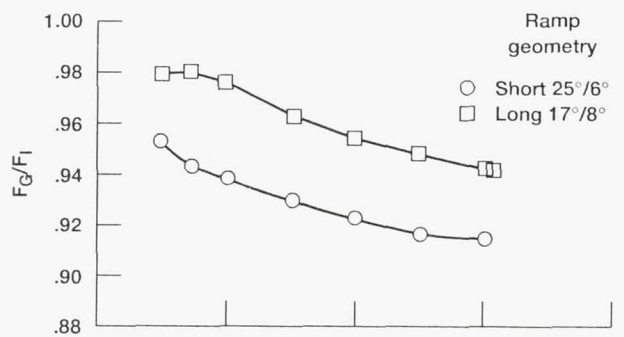
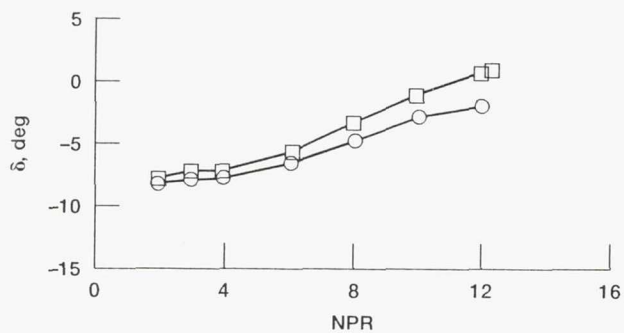


Figure 32.—Effect of ramp curvature on ramp centerline pressure distributions—long ramps.

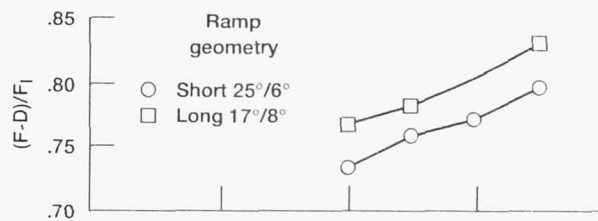


(a) Static thrust ratio.

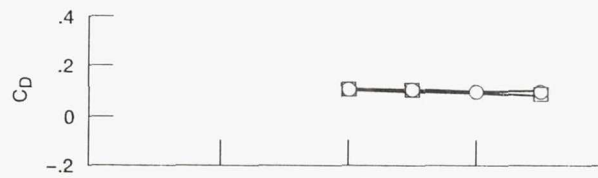


(b) Static thrust vector angle.

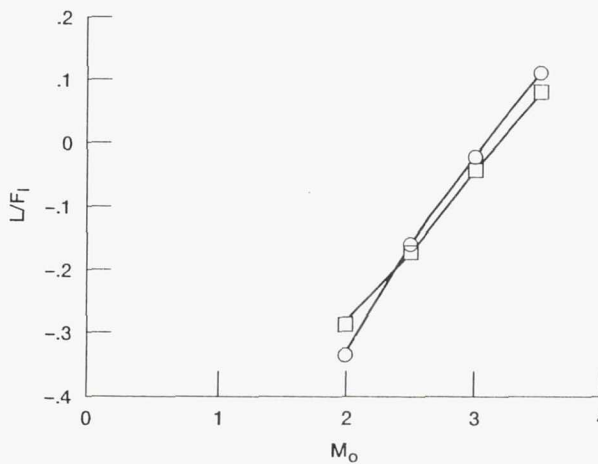
Figure 33.—Effect of ramp length on internal performance.



(a) Net thrust ratio at trajectory points (table 2).

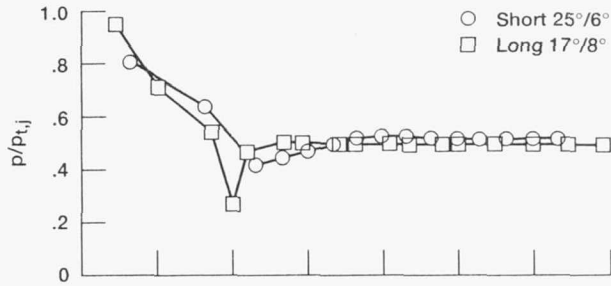


(b) Thrust-removed drag coefficient at trajectory points (table 2).

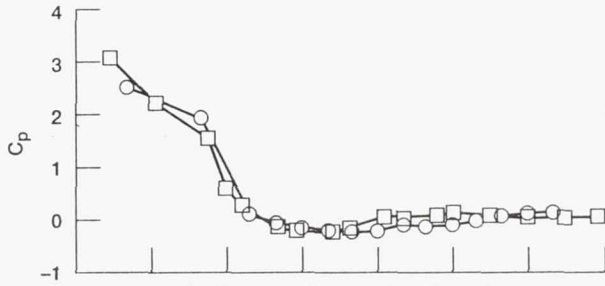


(c) Lift ratio at trajectory points (table 2).

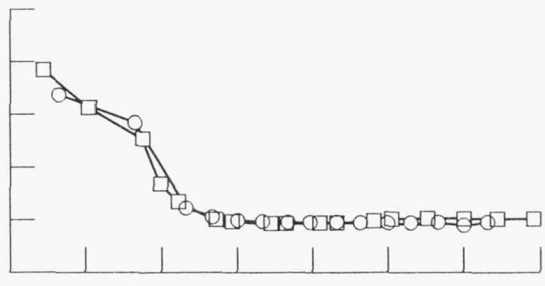
Figure 34.—Effect of ramp length on installed performance.



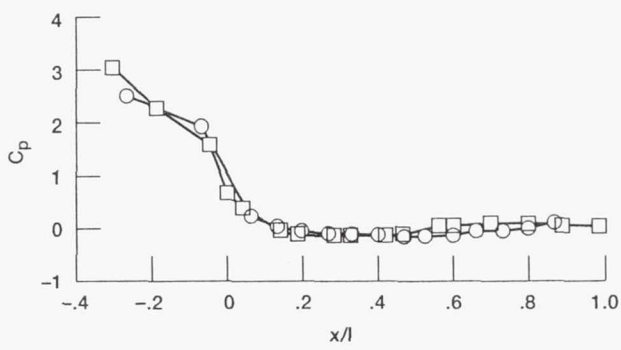
(a) Mach number = 0.0, NPR = 2.



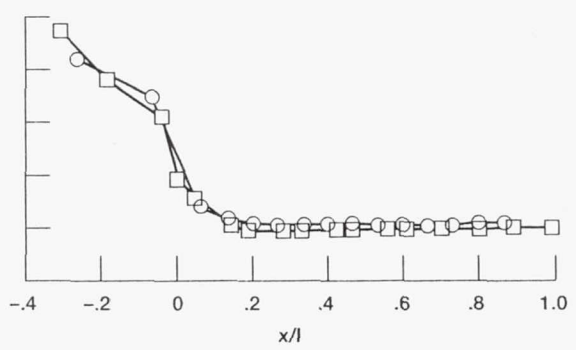
(b) Mach number = 2.0, NPR = 10.



(d) Mach number = 3.0, NPR = 20.



(c) Mach number = 2.5, NPR = 15.



(e) Mach number = 3.5, NPR = 35.

Figure 35.—Effect of ramp length on ramp centerline pressure distributions.

REPORT DOCUMENTATION PAGE

Form Approved
OMB No. 0704-0188

Public reporting burden for this collection of information is estimated to average 1 hour per response, including the time for reviewing instructions, searching existing data sources, gathering and maintaining the data needed, and completing and reviewing the collection of information. Send comments regarding this burden estimate or any other aspect of this collection of information, including suggestions for reducing this burden, to Washington Headquarters Services, Directorate for Information Operations and Reports, 1215 Jefferson Davis Highway, Suite 1204, Arlington, VA 22202-4302, and to the Office of Management and Budget, Paperwork Reduction Project (0704-0188), Washington, DC 20503.

1. AGENCY USE ONLY (Leave blank)	2. REPORT DATE October 1992	3. REPORT TYPE AND DATES COVERED Technical Memorandum	
4. TITLE AND SUBTITLE Supersonic Investigation of Two-Dimensional Hypersonic Exhaust Nozzles		5. FUNDING NUMBERS WU-763-01-21	
6. AUTHOR(S) Jeanne D. Carboni, Rickey J. Shyne, Laurence D. Leavitt, John G. Taylor, and Milton Lamb		7. PERFORMING ORGANIZATION NAME(S) AND ADDRESS(ES) National Aeronautics and Space Administration Lewis Research Center Cleveland, Ohio 44135-3191	
8. PERFORMING ORGANIZATION REPORT NUMBER E-7067		9. SPONSORING/MONITORING AGENCY NAMES(S) AND ADDRESS(ES) National Aeronautics and Space Administration Washington, D.C. 20546-0001	
10. SPONSORING/MONITORING AGENCY REPORT NUMBER NASA TM-105687		11. SUPPLEMENTARY NOTES Jeanne D. Carboni and Rickey J. Shyne, NASA Lewis Research Center, Cleveland, Ohio. Laurence D. Leavitt, John G. Taylor, and Milton Lamb, NASA Langley Research Center, Hampton, Virginia 23665-5225. Responsible person, Jeanne D. Carboni, (216) 433-3946.	
12a. DISTRIBUTION/AVAILABILITY STATEMENT This report contains information which falls under the purview of the U.S. Munitions List, as defined in the International Traffic in Arms Regulations. It shall not be transferred to foreign nationals in the U.S., or abroad, without specific approval. Penalty for violations is described in ITAR, Section 127. Subject Category 07		12b. DISTRIBUTION CODE	
13. ABSTRACT (Maximum 200 words) An experimental investigation was conducted in the NASA Lewis Research Center 10-Foot by 10-Foot Supersonic Wind Tunnel to determine the performance characteristics of two-dimensional hypersonic exhaust nozzles/afterbodies at low supersonic conditions. Generally, this type of application requires a single expansion ramp nozzle (SERN) that is highly integrated with the airframe of the hypersonic vehicle. At design conditions (hypersonic speeds), the nozzle generally exhibits acceptable performance. At off-design conditions (transonic to mid-supersonic speeds), nozzle performance of a fixed geometry configuration is generally poor. Various two-dimensional nozzle configurations were tested at off-design conditions from Mach 2.0 to 3.5. Performance data is presented at nozzle pressure ratios from 1 to 35. Jet exhaust was simulated with high-pressure air. To study performance of different geometries, nozzle configurations were varied by interchanging the following model parts: internal upstream contour, expansion ramp, sidewalls, and cowl.			
14. SUBJECT TERMS Hypersonic nozzles; Nonaxisymmetric nozzles; Two-dimensional nozzles; Single-expansion ramp nozzles		15. NUMBER OF PAGES 46	
16. PRICE CODE A03		17. SECURITY CLASSIFICATION OF REPORT Unclassified	
18. SECURITY CLASSIFICATION OF THIS PAGE Unclassified		19. SECURITY CLASSIFICATION OF ABSTRACT Unclassified	
20. LIMITATION OF ABSTRACT			